Maria Beatriz Queiroz de Andrada Bruxelas

Licenciada em Engenharia de Micro e Nanotecnologias

Nickel - 3 Yttria Stabilized Zirconia - Graphite Electrical Energy Storage Device

Dissertação para obtenção do Grau de Mestre em
Engenharia de Micro e Nanotecnologias

Orientador: Isabel Maria das Mercês Ferreira, Professora Associada, Faculdade de Ciências e Tecnologia da Universidade Nova de Lisboa

Júri:

Presidente: Professor Hugo Manuel Brito Águas, Ph.D.

Arguente: Professor Rui Alberto Garção Barreira do Nascimento Igreja, Ph.D.

Vogal: Professora Isabel Maria das Mercês Ferreira, Ph.D.

FACULDADE DE CIÊNCIAS E TECNOLOGIA
UNIVERSIDADE NOVA DE LISBOA

Setembro 2017

Nickel - 3 Yttria Stabilized Zirconia - Graphite Electrical Energy Storage Device

Faculdade de Ciências e Tecnologia

Universidade Nova de Lisboa

AGRADECIMENTOS

A meio da tese já tinha noção que tinha que agradecer a muita gente o facto de esta estar terminada. Foi escrita pela minha mão, mas com a contribuição de muitos. Podia muito bem dizer que fui maestro de uma orquestra bem orquestrada, a bem ou a mal. Se há coisa de que me orgulho, como bom português, é de ser desembaraçada. Mas o meu desembaraço só deu frutos com muita ajuda e boa vontade por parte dos meus colegas, amigos e professores.

Primeiro, à professora Isabel por ouvir muitas das minhas ideias descabidas e por me apoiar em quase todas elas! À Ana Baptista, minha ex-orientadora de estágio pelos bons conselhos. À Ana "do RAMAN" por ter concedido que tantas amostras fossem analisadas. A todos os meus colegas de laboratório, que estão sempre dispostos a ajudar: ao David que faz questão em discutir tudo o que eu digo com a calma de um eremita budista, à Filipa, que reitera o que eu digo ao David de uma forma que ele compreenda; ao João, que se ofereceu para lidar sozinho com "os putos da Ciência Viva" e me orientou na caracterização dos meus dispositivos; à Ana Gaspar, que assistiu ao filme que foi a Zircónia, literal e metaforicamente; ao Guilherme pelo seu *input*, a sua panca pela "uniformidade" e o péssimo hábito de dizer "Oh colega!". À Inês, que me encontra tudo no laboratório; ao Almeida por toda a disponibilidade; ao Jaimito porque ajuda em tudo o que pode e manda aquelas piadas secas e também à Tabby-chan por ser uma amor de pessoa e por me fazer rir com as dificuldades.

Este trabalho realizou-se também graças a outros professores e investigadores do Departamento de Ciências dos Materiais (DCM) que me acompanharam durante a minha (demasiado longa) vida académica: Ao professor Alexandre Velhinho, que me cedeu lixas aquando da minha cruzada de esfoliação. Ao professor Paulo Borges, por me ter deixado meter grafite no forno de biomateriais sem fazer grande alarido (podia ter corrido melhor). À professora Regina Monteiro que me elucidou quanto aos cerâmicos; à Andreia e aos meus *guys* do laboratório de Cerâmicos e Vidros, Daniel e Dmytro que aturaram "eu e prensa a prensa e eu" durante tantos dias. Também ao Alex, ao Paul e ao Prof. Carlos Dias, sem os quais não tinha conseguido desenvencilhar-me com o EIS, e sem dúvida ao Professor Nuno Paulino, do Departamento de Eletrónica, que me ajudou a interpretar os meus resultados. Sem estar a contar, tenho mais alguns agradecimentos bem merecidos a conceder: ao Prof. Robert Wiley, da Vicarte, por partilhar o seu tempo e conhecimento sobre refratários e por me apresentar a quem mais me pudesse ajudar. Ao Prof. António Matos, que me autorizou a utilizar o forno para coisas "não tão bio". E claro, ao sempre-disponível Prashant Dabas, que demonstrou tanto interesse pelo meu trabalho e arranjou espaço para as minhas coisas, num calendário bem preenchido.

Também, aos meus amigos e a todo aquele bom pessoal do CENIMAT (Cristina, João, Roger! …e a ti também Bea Coelho). Kelly Barras e Tiago senti que os meus problemas eram vossos! Aninhas, a ti por todos aqueles "*Tu vais conseguir*". Aos outros palermas de ambiente (Miguel, Diogo, Flávia, Nuga) só vos tenho a dizer "*A história não acaba aqui". Last but not least,* Daniel Vicente por teres estado lá para mim durante os últimos três anos e por sempre me teres empurrado para a frente! Sem esquecer, à minha família, que me acompanhou durante tantos anos e principalmente, à minha mãe, pelo suor que foi criar este bem precioso! Se há razão para chegar onde cheguei, essa razão és tu. Já não tenho que levar com a piada do "Acaba o curso quando eu já for velha". Com efeito, já não era sem tempo.

ACKNOWLEDGMENTS

Halfway my dissertation I was already much aware that I would had to thank many people for the fact that it would be finished on time. It was written by me, but with the contribution of many. I can surely say I was the conductor of a well-orchestrated orchestra, rightly or wrongly. If there is something I'm proud of, as a Portuguese, is of being resourceful. But my resourcefulness was only of service with the help and good-will of my colleagues, friends and professors.

First, to Professor Isabel, for hearing my foolish ideas and for having supported me in most of them! To Ana Baptista, for the good advice. To Ana "of RAMAN" that allowed for a lot of samples to be analyzed (caught the joke?). To all my lab colleagues, who are always willing to help: to David, who makes a point of discussing everything that I say with the calmness of a Buddhist Hermite; to Filipa, that reiterates what I tell David in a way that he can understand; to João that dealt all-alone with the Ciência Viva kids and oriented me in the characterization of my devices; to Ana Gaspar, that assisted my troublesome zirconia crusade; to Guilherme, for his input, his obsession with uniformity and his awful habit of saying "Oh colega". To Inês, who always finds everything in the lab, to Almeida for being always available, to Jaime because he helps in everything he can and tells terrible jokes and to Tabby-chan, for being such a lovely person and for making laugh of challenges.

This work was done with the help of other professors and investigators at the Material's Department (DCM) whom accompanied my (lasting) academic life. To Professor Alexandre Velhinho, that spared me some materials for the exfoliation process. To Prof. Paulo Borges, for letting me put graphite in the biomaterials' furnace without making a fuss (It could have worked better). To Prof. Regina Monteiro that elucidated me about ceramics, to Andreia and the guys from the Ceramics' and Glasses' Laboratory, Daniel and Dmytro, that kept up with "me and the press, the press and me" for so many days. Also, to Alex, Paul and to Prof. Carlos Dias without whom I could never have made it with EIS, and without a doubt to Prof. Nuno Paulino, from the Electronics Department, who helped me to interpret my results. I have other well-deserved acknowledgements to concede: to Professor Robert Wiley from Vicarte, for sharing his time and knowledge of refractories and for introducing me to others who could help me: to Professor António Matos, who authorized me to use Vicarte's furnace and to Prashant Dabas, who demonstrated so much interest in my work and who made room for my stuff in a fully scheduled calendar.

Also, to all my friends and all the good people of CENIMAT (Cristina, João, Roger! Bea Coelho). Kelly Barras and Tiago, I felt my problems were yours too! Aninhas, to you, for all those "You can do it!". To those environment fools (Miguel, Diogo, Flávia, Nuga), I'll just say "The journey doesn't end here". Last but not least, to Daniel Vicente for being there for me in the last three years and for always pushing me forward! And of course, to my family, who accompanied me for so many years and mainly to my mother, for all her hard-work in raising me so well! If there is a reason I'm here, that reason is you. I won't have to be stuck with that dark humor of yours "When you end it, I'll be old". As a matter of fact, it was time.

ABSTRACT

A Nickel-3 Yttria Stabilized Zirconia-Graphite Electrical Energy Storage (EES) device was fabricated using porous 3% mol Yttria-Stabilized Zirconia (3YSZ) as the separator and potassium hydroxide (KOH) as the electrolyte. The porous separator was fabricated through uniaxial pressing of 3YSZ nanopowder mixed with solid particles of Poly-vinylidene fluoride (PVDF) with a ratio of 2:1.5, respectively, to obtain maximum open porosity (59%). The resulting pellet was sintered using 2 ºC/min heating ramp (from 25 ºC to 1100 ºC) with a two-hour platform at this same temperature. Chemical exfoliation of graphite powder into graphene was performed mixing graphite powder in 25% water and 75% acetone solution (particle concentration of 3 mg/ml), that undergone a four-hour ultrasonication bath. The liquid phase of this solution was then evaporated at room temperature (RT). In order to determine qualitatively the amount of graphene present in the exfoliated graphite powder obtained, peak intensity ratios of its Raman spectrum were determined (I_{2D}/I_G=0.90, I_D/I_G=0.85), revealing the presence of multilayer graphene. To fabricate the exfoliated graphite electrode, the powder was mixed with a binder consisting of PVDF dissolved in N,N-Dimethylfomammide (DMF) in a proportion of 1:10 w/v, respectively. A ratio of 1:5 exfoliated graphite to binder was used to attain a maximum conductivity of $(1.17 \pm 0.18) \times 10^3$ S/m, a concentration of majority carriers of -5.22×10^{17} cm^{-2} and a mobility of 1.98 $cm^2/V{\cdot}s$, all for a percentage of active material of only 27.93%. The nickel electrode was obtained from a commercial source, being that both electrodes were deposited on opposing sides of the separator by drop casting, and left to dry at RT. The performance of the device was measured by Cyclic Voltammetry (CV), galvanostatic Constant Current Cyclic Charge Discharge (CCCD), Constant Current Discharge (CCD) and Electrochemical Impedance Spectroscopy (EIS), from which it was possible to design an Electrical Equivalent Circuit (EEC) based on the Randles Cell and to determine the Equivalent Series Resistance (ESR), 63.55 Ω ± 8.62 Ω. The analysis of the data allowed to attest the high non-linearity of the device, that demonstrated to have a high capacitance (0.99 Fg^{-1}) and a calculated energy and power densities of 0.31 $Wh{\cdot}kg^{-1}$ and 10.29 µWh cm^{-2}.

Keywords: Electrical Energy Storage, Supercapacitors, Porous 3% mol Yttria-Stabilized Zirconia (3YSZ), Chemical exfoliation of graphite, Nickel electrode.

RESUMO

Foi fabricado um dispositivo de armazenamento elétrico constituído por um elétrodo de grafite esfoliada e por outro de Níquel e um separador poroso de Zircónia dopada com 3% mol de Ítria (3YSZ), impregnada em hidróxido de potássio (KOH). O separador poroso foi fabricado através da prensagem uniaxial de nanopó de 3YSZ misturado com partículas sólidas de fluoreto de polivinilideno (PVDF) com uma proporção de 2:1,5, respetivamente, de modo a obter uma porosidade aberta de 59%. A pastilha resultante foi sinterizada usando uma rampa de aquecimento de 2 ºC/min (de 25 ºC a 1100 ºC) com uma plataforma de duas horas a esta mesma temperatura. A esfoliação química de pó de grafite em grafeno foi feita numa solução de 25% de água e 75% de acetona, que foi submetida a um banho de ultrassons durante 4 h, deixando-se depois evaporar a fase líquida à temperatura ambiente. Para determinar qualitativamente a quantidade de grafeno presente no pó de grafite esfoliado, as razões de intensidade dos picos do seu espectro Raman foram determinadas (I_{2D}/I_G=0,90, I_D/I_G=0,85), revelando a presença de grafeno multicamada. Para fabricar o elétrodo de grafite esfoliada, este foi misturado com um ligante constituído por PVDF dissolvido em N, N-Dimetilfomammida (DMF) numa proporção de 1:10 w/v, respetivamente. Uma proporção de grafite esfoliada de 1 para 5 de ligante foi utilizada para alcançar uma condutividade máxima de (1,17±0,18) x 10^3 S/m, uma concentração de portadores maioritários de -5,22 x 10^{17} cm^{-2} e uma mobilidade de 1,98 $cm^2/V{\cdot}s$, tudo para uma percentagem de material ativo de apenas 27,93 %. O elétrodo de níquel foi obtido a partir de uma fonte comercial, sendo que ambos os elétrodos foram depositados em lados opostos do separador por *drop casting* e deixados a secar à temperatura ambiente. O desempenho do dispositivo foi medido por Voltametria Cíclica (CV), Carga-Descarga a Corrente Constante (CCCD), Descarga a Corrente Constante (CCD) e Espectroscopia de Impedância Eletroquímica (EIS), a partir do qual foi possível construir um Circuito Equivalente Elétrico (EEC) com base na célula de Randles, e determinar a resistência em série equivalente (ESR), 63,55 Ω ± 8,62 Ω. A análise dos dados permitiu atestar a alta não-linearidade do dispositivo, que demonstrou ter uma capacitância elevada (0,99 Fg^{-1}) e uma densidade de energia e potência de 0,31 $Wh{\cdot}kg^{-1}$ and 10,29 µWh cm^{-2}, respetivamente.

Palavras-chave: Dispositivos de Armazenamento de Energia, Supercondensadores, Zircónia porosa dopada com 3% mol de Ítria (3YSZ), Esfoliação química da grafite, Elétrodo de Níquel.

LIST OF ABBREVIATIONS

AC	– Activated Carbon
2D	– two-dimensional
BET	– Brunauer–Emmett–Teller theory
CCCD	– Constant Current Charge Discharge
CDC	– Carbide-derived carbon
CNTs	– Carbon nanotubes
CPE	– Constant Phase Element
CSZ	– Cubic Stabilized Zirconia
CV	– Cyclic Voltammetry
DL	– Double Layer
EC	– Electrochemical Capacitor
EDL	– Electrical Double-Layer
EDLC	– Electrochemical Double-Layer Capacitor
EDR	– Equivalent Distributed Resistance (EDR)
EEC	– Electrical Equivalent circuit
EES	– Electrical Energy Storage
EIS	– Electrochemical Impedance Spectroscopy
EDLC	– Electrochemical Double-Layer Capacitor
ESR	– Equivalent Series Resistance
ESS	– Energy Storage Systems
FSZ	– Fully Stabilized Zirconia
FWHM	– Full Width at Half Maximum
HSC	– Hybrid Supercapacitor
ILs	– Ionic Liquids
IR drop	– Internal Resistance drop
KOH	– Potassium Hydroxide
LIB	– Lithium Ion Battery
OCV	– Open Circuit Voltage
OER	– Oxygen Evolution Reaction
PANI	– Polyaniline
PC	– Pseudocapacitor
PC	– Propylene carbonate
PPy	– Polypyrrole
PSD	– Pore Size Distribution
PSZ	– Partially Stabilized Zirconia
PTFE	– Polytetrafluoroethylene

PTh – Polythiophene

PVA – Polyvinyl alcohol

PVDF – Poly-vinylidene fluoride

rms – Root mean square

SEI – Solid-Electrolyte Interface

SSA – Specific Surface Area

VOC – Volatile Organic Compounds

XRD – X-Ray Diffraction

YSZ – Yttria Stabilized Zirconia

LIST OF SYMBOLS

θ – Angle

ρ – Resistivity

σ – Conductivity

σ_i – Ionic conductivity

ω – Angular frequency

C_{dl} – Double-layer Capacitance

C_s – Specific Capacitance

E_D – Energy Density

P_D – Power Density

C_s – Specific Capacitance

$NIMH_x$ – Nickel-Metal Hydride

Y_2O_3 – Yttrium Oxide

P_D – Power Density

E_D – Energy Density

τ – Time constant

$P_{máx}$ – Maximum power

I_{max} – Maximum Current

TABLE OF CONTENTS

LIST OF FIGURES

LIST OF TABLES

1. Motivation and objectives

1.1. Motivation

There is no doubt about the relevance of Electrical Energy Storage (EES) in today's world and in what could bring to the future of energy. Many efforts have been made by several countries to transition from fossil fuels to renewable energies. Powering the electric grid and fabricating efficient and capable EES would allow for sustainable public transportation. Investment in these systems is of great interest for the private sector, namely the automotive industry, that every year has an even broader offer of hybrid and all-electric vehicles. The development of competitive EES and associated technologies is essential for the future of the grid.

The classification of EES can be categorized by how energy is stored in the system and the device configuration. Generally electrical EES can be distinguished by two charging storing mechanisms: capacitive charge storage (capacitors, supercapacitors) or electrochemical charge storage (conventional rechargeable batteries and flow batteries) [1]. In general, batteries are used for their relatively high energy density and supercapacitors for their high power density, however, neither of them can fully meet the needs of practical applications [2], which means the two devices play complementary functions when they are hybridized [3]. The ideal would be to have high-power, high-energy device. Whether to approach these goals by increasing the power density of battery materials or increasing the energy density of supercapacitors is one of the enticing features of the field [4].

In batteries, heterogeneous charge-transfer and chemical phase changes introduce relatively slow steps into the process of energy storage and delivery [5], in addition they generate Joule and thermochemical heating during operation. Such heat, if not dissipated, will effectively result in overheating, thermal runaway and even fire. Moreover, changes in electrode volume (swelling and shrinking) that occur during charge and discharge cycles damages the structure and gives rise to poor mechanical/cycling stability, to a short cycle life (that is also limited due to the lack of fully reversible redox reaction) and poor electrical conductivity of the electroactive materials confining fast electron transport (low power density) [2], [10].

Also, high-rate charging in a battery would give rise to a high underpotential due to electrochemical kinetics through a polarization resistance. This rate limitation results in undesirable metal-plating, a degradation and failure mechanism in batteries that can lead to short circuits, uncontrollably energetic chemical reactions and ultimately deterioration of the cell performance [6]. With respect to power and energy performance, the power capability of the battery is not symmetric for charge and discharge unless the battery is maintained at a specified partial state-of-charge (typically 60–70%) [7]. In most applications, it is common that only a relatively small fraction (less than 10%) of the energy capacity of a high power battery is used in order to achieve high cycle life (100,000–200,000 cycles) [6].

By contrast, supercapacitors can deliver high power in very high rates since the mechanism of energy storage it is inherently rapid: it simply involves charge-separation and the movement of ions to and from electrode surfaces [5]. Its charge storage mechanism is also the reason it has a robust cycle life. It also has the advantage of having a broader temperature window of stable operation with high power performance down to -40 °C [2]. Hence, in recent years, supercapacitors became an important development in the field of energy storage and conversion [8] and that is why tremendous research effort has been aimed at increasing the energy density of supercapacitors without sacrificing high power capability (so that they reach the levels achieved in batteries) and at lowering fabrication costs [9].

Nowadays, from a practical point of view, the most important challenge is to increase the energy density higher than 10 Wh kg^{-1} with low fabrication cost while using environmentally friendly materials [9], maintaining the high power density (at least 500 W/kg) and at least 500,000 deep discharge cycles [7]. Baring this is mind, the focus of this exploratory work is to design, fabricate and characterize a EES device with possible application for the future of the power supply.

1.2. Objectives

The final purpose of this dissertation is to assemble an EES device using nickel and exfoliated graphite as the positive and negative electrode, respectively, a separator made of porous 3% mol Yttria-Stabilized Zirconia (3YSZ) and to study its electrical performance by Cyclic Voltammetry (CV), Electrochemical Impedance Spectroscopy (EIS) and galvanostatic Constant Current Cyclic Charge Discharge (CCCD), using potassium hydroxide (KOH) in a concentration of 6 M, as an electrolyte.

Specific objectives are the chemical exfoliation of graphite into graphene for its use on the carbon-based electrode and fabricating porous 3YSZ pellets by uniaxial pressing and sintering, controlling the porosity by the addition of particles of solid polymers: Poly-vinylidene fluoride (PVDF) and of Polyvinyl alcohol (PVA). The presence of graphene after chemical exfoliation will be determined by Raman Spectroscopy, the conductivity of the carbon-derived electrode by 4 point-probe and the mobility of majority carriers by measuring the Hall-effect. Finally, the open porosity of the 3YSZ pellets after sintering will be determined by the Archimedes Principle.

2. GENERAL INTRODUCTION

2.1. Electrical Energy Storage and its charge storage mechanisms

All Electrical Energy Storage (EES) devices share a similar structure, they are typically composed by a positive and a negative electrode, that have in between an ion-permeable separator impregnated in a liquid electrolyte, as schematized in Fig.1. The electrodes can be metals or porous composites (65-75% open porosity) with a thickness that generally ranges between 100 and 300 μm [10]. Carbon composites contain, besides the active material (a carbon powder), polymeric binders to hold the powder structure together and conductive diluents (e.g. carbon black) so that electrons can be transported from the active material to the current collector [5], [10], [11]. The electrochemically inert binding agent can be an organic paste-forming liquid such as nujol and paraffin oil or polymeric binders such as polytetrafluoroethylene (PTFE), that are often used nowadays [12], [13]. For avoiding unwanted particle contact resistance, the binder must be well distributed and used sparingly to avoid the formation of an electrically insulating layer between the carbon particles. The current collectors are typically metals and must not react with the electrode materials. Typically, copper is used for the positive electrode and aluminum for the negative electrode [5], [11].

As reactions at the anode usually take place at lower electrode potentials than at the cathode, the terms negative and positive electrode are used. The more negative electrode is designated the anode, whereas the cathode is the more positive one [14]. The types of materials chosen for the device and the interactions between them will determine the charge storage mechanism, its performance and ultimately its classification. Generally, three types of charge storage can be distinguished: capacitive, pseudocapacitive and Faradic (or electrochemical).

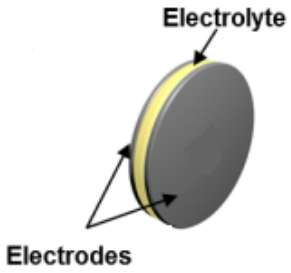

Figure 1 Schematic of a EES device

Capacitive charge storage

Capacitive charge storage is typical of Electrostatic, Electrolytic and Electric Double Layer Capacitors (EDLCs). In Electrostatic Capacitors there is a thin dielectric separator (e.g. ceramic, glass or plastic film) in between the two metal electrodes. Here, the energy is stored in the electrical field originated by the charge separation. An electrolytic capacitor is similar in construction to an electrostatic capacitor but the separator is impregnated with a ionic conductive electrolyte [15].

On the other hand, EDLCs store energy in the electrical double-layer (EDL)[1], which is the charge separation between an electrode space charge and a layer of electro-adsorbed ions at the interphase between electrode and electrolyte solution. When a voltage is applied across these electrodes the electrolyte ions of the opposite sign accumulate on the surface of each electrode. Although this storage mechanism is the same as that in the electrolytic capacitors, the specific capacitance (C_s), in [Fg^{-1}],

[1] There are several models that describe charge separation at the electrode/electrolyte interface when an electrode is polarized: The Helmholtz Model, the Gouy and Chapman Model, and the Stern Model, which accounts for the more variables. All these models are described by [3][45].

increases drastically due to the high porosity and large specific surface area (m^2g^{-1}) of the electrode (e.g. activated carbon) [8], [9], [11]. No redox reactions occur, so the response to changes in potential without diffusion limitations is rapid and leads to high power. However, the charge is confined to the surface, so the energy density is less than that of batteries [4].

Faradic (electrochemical) charge storage

In general, faradaic processes represent electron transfer reactions at the interface between an electrode and its contacting solid or liquid electrolyte phase, that is able to accept or donate electrons [8]. Faradic charge storage derives from diffusion controlled processes such as electrosorption, intercalation and redox reactions that occur in the bulk of batteries' electrodes, so these processes can be slow. The reversible multi-electron redox faradaic reactions lead to mechanical changes, making the electrodes swell and shrink in the charging/discharging cycles. These changes in volume damage the structure and give rise to poor mechanical/cycling stability, leading to lower cycle life and poor electrical conductivity of the electroactive materials confining fast electron transport (low power density) [2], [11].

Pseudocapacitance (Capacitive faradic storage)

Pseudocapacitance is generally described as a result of fast surface faradaic processes that arise from electrosorption of ions, accompanied by surface redox reactions, in which electrons transfer occur crossing the interface of the current collector and active materials [8]. These processes result in a capacitance that, while often large, is not electrostatic in origin (hence the 'pseudo' prefix to provide differentiation from electrostatic capacitance). It can also take place across the electrode/electrolyte interface in lesser extent in supercapacitors [2], [11].

Faradic Pseudocapacitance can occur as a result from the following three mechanisms: underpotential deposition, redox pseudocapacitance and intercalation pseudocapacitance. Underpotential deposition occurs when metal ions form an absorbed monolayer on a different metal's surface well above their redox potential. The intercalation pseudocapacitance is based on the intercalation of electroactive species (adsorption/insertion) at/near the electrode surface without crystallographic phase change. Fig. 2 represents the correlation between the three charge storage mechanisms [16].

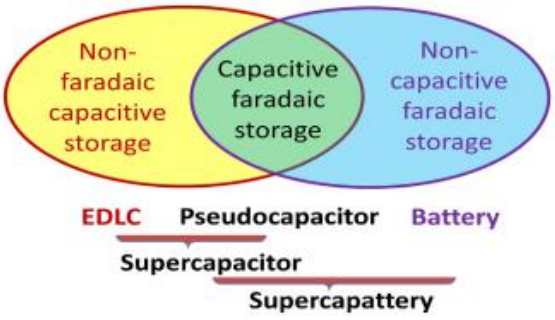

Figure 2 Schematic correlation between EDL capacitor, pseudocapacitor, battery and supercapattery (= hybrid of supercapacitor and battery) in terms of capacitive and faradaic charge storage processes [8].

In some cases, some materials do not show pseudocapacitance in bulk, but do so in nanostructured states. This kind of material is called an extrinsic electrode material. Otherwise, materials display the characteristics of capacitive charge storage for a wide range of particle sizes and morphologies and they are called intrinsic materials [17].

2.2. Supercapacitors

The capacitance of a conventional capacitor typically ranges between 10^{-6}–10^{-2} F, therefore, the energy stored in a capacitor is too small for meaningful practical uses. For example, for a 50 mF capacitor with an applied voltage of 100V, the energy stored is only 250 J [8]. Supercapacitors, also called 'ultracapacitors' or electrochemical capacitors (ECs) have greater capacitance per unit volume due to their porous electrode structure (compared to electrostatic and electrolytic capacitors) and to the very small separation between the electronic and ionic charge at the electrode surface. They can be divided in (1) Electrical double layer capacitors (EDLCs) (2) Redox supercapacitors or Pseudocapacitors (3) Hybrid supercapacitors (HSCs) or Asymmetric Supercapacitors [2].

'Pure' EDLCs, in theory, have not a faradic charge storage mechanism, however, many carbon electrode materials contain functional groups on their surfaces which may exhibit electrochemical interactions with selected electrolytes, therefore, pseudocapacitance may complement previously described electrostatic ion adsorption of an ideal EDLC. When ion adsorption sites have a very broad distribution of enthalpies, the concentration of electro-adsorbed ions follows a linear dependence on the applied voltage for a wide range of concentrations, as typically observed in some pseudocapacitive materials and in EDLCs [11].

Pseudocapacitive materials hold the promise of achieving battery-level energy density (also higher specific capacitance) combined with the cycle life and power density of EDLCs [4], however, they usually suffer from low electrolyte-accessible surface area and low conductivity, which leads to a large Equivalent Series Resistance (ESR) [17]. Generally, the faradaic processes taking place on the electrode materials mainly involve the following types: (1) Reversible adsorption (2) Redox reactions of transition metal oxides (3) Reversible electrochemical doping/dedoping in electrically conducting polymers and (4) Doping of function groups/heteroatoms (including N, O, S, B, and P) to carbon materials [9]. The most commonly investigated classes of pseudocapacitive materials are transition metal oxides/hydroxides (i.e., RuO_2, Mo_xN or MnO_2) and conducting polymers, but other well-known examples are metal sulfides, metal nitrides and carbides [4], [6], [17].

The most investigated insertion-type electrodes involving intercalation pseudocapacitance are V_2O_5 and Nb_2O_5 (they allow high energy density and wide potential window and are promising candidates as anode materials [4]. Redox and intercalation pseudocapacitances are more frequently exploited in the design of PCs since they display very fast charge/discharge rates without diffusion limitation. This is the most obvious distinction from batteries, which are limited by solid-state diffusion and suffer from a poor cycling rate [15], [17]. Conducting polymers usually used are polyaniline (PANI), polypyrrole (PPy) or derivatives of polythiophene (PTh), because of their excellent conductivity, ease of synthesis, low cost and high specific capacitance [4]. The redox process is used in conducting polymers to store and release charge. When oxidation occurs, (also referred to as 'doping'), ions are transferred to the polymer backbone. When reduction occurs ('de-doping') the ions are released back into the solution. Charging in conducting polymer films takes place throughout the bulk volume of the film and not just on the surface, as is the case with carbon [15].

Hybrid Supercapacitors (HSCs), also called Asymmetric Supercapacitors (ASCs) are composed of an EDLC electrode (capacitive electrode as the power source) and a pseudocapacitive or battery type electrode (faradic electrode as the energy source), combining the properties of both systems and leading to an intermediate performance [6], [9]. The HSCs' electrodes operate reversibly in different potential ranges with different electrochemical mechanisms, thus increasing the operation voltage and leading to the improvement in energy density while maintaining a high-power density [9]. One of the major issues for HSCs, however, is the imbalance in the charge/discharge rate between the two electrodes due to the intrinsic differences in the energy-storage mechanisms. This imbalance in the kinetics prevents full energy utilization of the intercalation electrode and imposes a high overpotential in the capacitive electrode, thus deteriorating the overall efficiency [17]. Although symmetric supercapacitor devices (EDLCs) still demonstrate better power performance and consequently play a dominant role in the market [6], the intriguing features of aqueous HSCs have endowed them plenty of room to improve their performances and to fulfill the ever increasing energy demands in future applications [9].

2.3. Carbon-derived electrodes

Carbon has four crystalline (ordered) allotropes: diamond (sp^3 bonding), graphite (sp^2), carbyne (sp^1) and fullerenes. While two carbon allotropes are naturally found on earth as minerals, namely, natural graphite and diamond, the other forms of carbon are synthetic. Most of commercial carbons used today as an active material in electrodes are designated 'engineered carbons', manufactured carbons that have an amorphous structure with a more or less disordered microstructure based on that of graphite. Amorphous carbons can be considered as sections of hexagonal carbon layers with very little order parallel to the layers. The process of graphitization consists of the ordering and stacking of these layers into 'graphite' and is achieved by high-temperature treatment (>2500 °C). Between the extremes of amorphous carbon and graphite, a wide variety of carbon materials can be prepared and their properties tailored, to some extent, for specific applications [2].

A variety of porous forms of carbon are currently preferred as the electrode materials because they have exceptionally high surface areas, relatively high electronic conductivity and acceptable cost. More than 80% of the commercially manufactured supercapacitors are based on EDLCs using carbon as the electrode material and a big percentage of the remaining 20% based on carbon allotropes. The first 80% include activated carbon (AC), carbon nanotubes (CNTs), carbon onion, templated carbon, etc. Among all materials, AC is the most used, due to its high availability, low cost and high specific surface areas (SSA).

It has been demonstrated both theoretically and experimentally that several factors significantly affect the electrochemical performances of carbon materials including (1) SSA (2) Electrical conductivity (3) Pore size distribution (PSD) (4) Pore size/volume (5) Surface functionalities (heteroatoms doping) and (6) Interlayer distance [2]. The accessibility of the pores to the electrolyte it is extremely important for a good overall performance. The mobility of the ions within the pores is different from the mobility of ions in the bulk of the electrolytic solution and is greatly influenced by pore size, that must be adequate to the electrolyte used [15]. It was proved experimentally that pore sizes very close to those of the ion sizes could result in the maximum double-layer (DL) capacitance in carbon-derived carbides (CDC) and that larger and smaller pores lead to a significant drop in capacitance [10].

With higher SSAs there are more active sites for charge-transfer reactions and for ion adsorption (formation of an EDL), resulting in enhanced specific capacitance. However, the presence of oxygen, nitrogen, and other atoms in its amorphous structure leads to limited conductivity. Activated forms of carbon have Brunauer–Emmett–Teller (BET) surface areas that range from 500 to ~3000m^2g^{-1}, where the last value exceeds theoretical surface area of a perfect single-walled graphene. This is due to the formation of vacancies within individual graphene layers that allow nitrogen adsorption on the edges of graphene segments. In addition, the small size of particles buffers the stress from the expansion and shrinkage of the electrodes during the charge/discharge, when electrochemical reactions are involved, preventing the pulverization of the electrode and improving the cycle stability [2]. Nonetheless, the wide PSD of ACs means that their high SSA cannot be fully exploited by the electrolyte to form the EDL (some pores are not accessible) which may limit the performance of the devices that use this material as an electrode. Despite this, most of other carbon structures [2], [10], [11] cannot match the gravimetric performance of ACs in comparable electrolytes since 2014: up to 250–300 Fg^{-1} in all electrolytes [11].

2.4. Graphite and graphene

Graphite is one of the most common allotropes of carbon and under standard conditions. Graphitic carbon surfaces can be regarded as being made up of (at least) two chemically different kinds of sites: basal and edge carbon sites, where the later are more reactive since they have unpaired electrons. The ratio of edge to basal sites generally increases with the degree of disorder. The specific DL capacitance can vary considerably and appear to be highly dependent on carbon morphology: DL capacitance of the edge orientation of graphite is reported to be an order of magnitude higher than that of the basal layer, so carbons with a higher percentage of edge orientations could be expected to exhibit a higher capacitance [2].

A single layer of graphite is called graphene. Graphene is a two-dimensional (2D) monoatomic thick building block of a carbon allotrope of sp^2-hybridized carbon atoms, with a honey-comb layer structure. [18]. Graphene proprieties include exceptional electron conductivity (10 times more conductive than

graphite), an electron mobility that is little affected by temperature (10 times higher than a commercial silicon wafer) and carriers with ballistic transport (mobility of 15000 $cm^2(V{\cdot}s)^{-1}$) under ambient condition. Despite having a tunable SSA (that goes up to 2670 m^2g^{-1}) [19]–[21] and of being chemically processable [22], its full potential for energy storage has not been fully developed [21]. Although graphene is one of the most promising electrode materials for supercapacitors, many challenges remain, particularly:

- To establish a standardized measurement of capacitor performance.
- To reduce the price of graphene-based EDLC.
- To understand the mechanism of ion sorption on graphene.
- To study self-discharge mechanisms of graphene-based supercapacitors.
- To propose a new storage method for graphene-based EDLCs, etc. [21].

Also, graphene sheets have a strong tendency to form irreversible agglomerates or even restack into graphite driven by the strong interlayer π-π stacking and Van der Waals interactions between the graphite single layers, leading to a greatly decreased accessible surface area and a limited ion diffusion rate. Therefore, the capacitance of current graphene-based electrode materials is generally far less than the theoretical gravimetric capacitance of about 550 Fg^{-1}, and the fast, reversible charge/discharge rates are still unsatisfactory for practical applications. Thus, graphene materials with single or few layers with less agglomeration are expected to exhibit high effective SSA and excellent electrochemical performance [23]. There are several approaches to inhibit the aggregation of graphene sheets that result in a mechanically jammed, exfoliated graphene agglomerate with very high surface area: (1) Incorporating pseudocapacacitive materials to form composites (2) Anchoring carbon nanostructures (carbon black) or metal nanoparticles on the edge planes of graphene sheets through ultrasonication approach, or even (3) Introducing solution-based spacers like water [9].

2.5. Nickel as a negative electrode

Nickel electrode, particularly nickel anode, is an efficient electro-catalyst and highly corrosion-resistant in alkaline medium [24]. A review of the literature furnishes a multiplicity of values for the normal potential of this element ranging from -0.138 V to -0.621 V, calculated to the standard hydrogen electrode as zero. Nickel is a very stiff metal, therefore, measurements made on any but finely divided nickel is apt to be affected by errors due to strain. Oxygen very certainly produces results that are too positive. Hydrogen, just as certainly, produces results that are too negative. In few cases were adequate precautions taken to insure absence of these gases, where the standard potential of nickel has been determined to be -0.231 V ± 0.002 V at 25 ºC [25]. Nevertheless, nickel alone is not what is commonly used as an electrode, but nickel hydroxide, which is a successful cathode material in Ni-Cd, Ni-Zn and Ni-Fe alkaline batteries, having a large area of application. It is also present in $Ni\text{-}H_2$ batteries which are extensively used in aerospace systems [26]. The positive electrode in NiFe cells is based on the nickel hydroxide/oxyhydroxide couple used in Nickel–Cadmium and Nickel-Metal Hydride ($NiMH_x$) cells. Two polymorphs of $Ni(OH)_2$ exist, they are α-$Ni(OH)_2$ and β-$Ni(OH)_2$; they can be transformed into γ-NiOOH and β-NiOOH, respectively. However, due to the low stability of α-$Ni(OH)_2$ in alkaline media, the β-$Ni(OH)_2$ is usually used as a precursor material in alkaline batteries [27]

Nickel is generally considered a suitable electrode material for the oxygen evolution reaction (OER) from concentrated alkaline solutions, as it is a highly chemically stable metal, i.e. corrosion resistant in the presence of concentrated KOH solution, and, it is relatively cheap. The OER has been investigated on a polished pure nickel anode in 30 wt% KOH solution under the temperature range 30-70 °C. The influence of electrochemically formed Ni(II) oxide on the nickel electrode was studied and it was found that Ni(II) oxide is being transformed to Ni(III) oxide due to the change in the valence state of active sites of the electrode material, so this can probably happen at room temperature in a smaller scale or even with a less concentrated KOH solution. With increasing temperature, both the oxidation and reduction peak potentials in voltammograms shift towards the positive direction and their potential difference lowers, which means that the equilibrium potential for oxygen evolution has been changed to a negative value [28].

2.6. Electrolytes and current collector

Cell voltage (V) is determined by the compatibility of the whole system, including the anode, cathode and electrolyte. In particular, the difference in chemical potential between the anode and the cathode is referred as the working voltage or operating voltage. Operating voltage is limited by the electrochemical window of the electrolyte, otherwise, the electrolyte will be reduced on the anode or oxidized on the cathode to form a passivating solid electrolyte interphase (SEI) film [29]. The SEI film remains impermeable to electrolyte solvent and prevents further electrolyte reduction, disrupting the formation of a double-layer and inducing resistance to the ion transport [11].

Also, power density depends upon the cell's ESR, which is strongly dependent on electrolyte conductivity [2]. Ideal electrolytes should fulfil the following requirements: (1) A wide voltage window (2) Excellent electrochemical stability (3) High purity (4) High conductivity [30] (5) High ionic concentration (6) Small solvated ionic radius (7) Low viscosity and (8) Environmental friendliness, low cost and easy availability. Electrolytes used in EES devices may be divided into three classes: aqueous, organic and ionic liquids (IL) [9]. Specifications of the three categories are depicted in Table 1.

Handling of aqueous electrolytes is easy and safe: they are non-flammable, can be easily produced on a large scale and used without the need of any particular conditions. They are constituted by solutions of acids (e.g. H_2SO_4), bases or alkalis (e.g. KOH) and salts [1]. For aqueous power sources, most electrode reaction potentials shift with pH variation according to the Nernst equation. The open circuit voltage (OCV) and working voltage change with pH since both positive and negative electrode reactions involve generation or consumption of protons [31]. Battery systems employing an aqueous electrolyte may be divided up into following subgroups (1) Strong acidic electrolyte (lead – acid batteries) (2) Weak acidic electrolyte (e.g., Leclanche batteries) (3) Neutral electrolyte (e.g., water activated systems) (4) Alkaline electrolyte (e.g., nickel – cadmium, alkaline manganese dioxide – zinc), where the prevailing electrolyte is potassium hydroxide (KOH), which have a pH > 14 and a conductivity of 0.6 Scm^{-1} for a 30 wt% of KOH [32].

On the other hand, organic electrolytes are typically prepared through dissolving organic salts in organic solvents and they are the most used in commercial devices. They are flammable (but much less than Lithium Ion Batteries (LIBs)), toxic, hygroscopic and must be handled in an atmosphere free of water and oxygen to ensure high voltage and excellent stability. Today, anhydrous acetonitrile (AN) and propylene carbonate (PC) are the state-of-the-art solvents used [1]. On the contrary, ILs present low flammability, but they are also hygroscopic, present low vapor pressure and are commonly employed at higher temperatures, still failing to meet the requirements for supercapacitors, that are mainly used in the temperature ranges of –30 to 60 °C in practical applications. In 2014, the operation voltage of carbon materials was improved to 4.3 V in organic solution through tuning the electrode potential by controlled electrochemical charge injection, maximizing the energy density of the supercapacitor by tenfold (to a level close to that of LIBs) without loss in power delivery or cyclic stability. This strategy could be applicable to supercapacitors based on other aqueous or non-aqueous electrolytes [11].

Table 1 Specifications of electrolytes uses in EES. Adapted from [1], [2], [6], [9], [11].

	Aqueous Electrolytes	Organic Electrolytes	Ionic Liquids (IL)
Cycle life	(-)	> 500000	(-)
BreakdownVoltage (Vb)	0.6 V – 1.4 V	2.3 V – 3 V	2.6 V – 4.0 V
Ionic concentration	High	Low	(-)
Viscosity	Low	High	High
Ion Size	Smaller than organic	Large	(-)
Ionic conductivity (RT)	≈ 1 Scm^{-1} (high)	low (order of magnitude lower comparing with aqueous)	several mS cm^{-1} (higher than organic)
Energy density	(-)	6 – 9 times that of the aqueous electrolyte.	Very high
Power density	Higher than organic electrolytes	Low	(-)
Cost	Very low	High	Prohibitively High

With aqueous electrolytes (strong acids (e.g., H_2SO_4) or bases (e.g., KOH)), corrosion-resistant current collectors are required (e.g. Au, Pt, Ti and stainless steel). These are more expensive and it is hard to decrease the interface ESR because they are not easily etched. In addition, graphite sheets and conductive carbon paper are widely used in practical application to reduce ESR, however, such collectors are mechanically fragile and cannot been freely bent to prepare flexible supercapacitors [9]. Other contributors to the ESR of supercapacitors include electronic resistance of the electrode material; interfacial resistance between the electrode and the current-collector [10]; ionic (diffusion) resistance of ions moving in small pores; ionic resistance of ions moving through the separator and electrolyte resistance [2]. In general, a small ESR is preferred for better electrochemical performance [33]. To obtain a low ESR the contact resistance between the active material coating and the current collector must be very low [10],[2].

With respect to the binder of the active material, it is of interest to know that the conductivity of a composite is directly related to the formation of a conductive network through the polymer matrix [34]. Second threshold percolation theory a composite becomes a conductor when particles can touch each other inside the material [35]. Particle contact resistance is highly dependent on both the physical morphology of the carbon particle (e.g., size, shape, aggregation, etc.) and the pressure that is applied to compact the particles. The calendaring process usually has two main purposes: porosity reduction and thickness control. The higher the compaction pressure the lower the resistance and only at high pressures the resistance of a packed powder begins to approach the resistivity of the bulk material. The effect of pressure is larger for smaller particles and generally results in thinner electrodes with low ESR. It must also be noted that a closely-packed structure also minimizes the amount of electrolyte contained in the inter-particle void space, so the density of the electrode needs to be carefully balanced against electrolyte requirements to avoid electrolyte-depletion effects [2].

2.7. Yttria Stabilized Zirconia (YSZ) as a porous separator

The separator prevents the occurrence of electron flow between the two electrodes, but it is ion-permeable, allowing ionic charge transfer to take place. Polymer or paper separators can be used with organic electrolytes and ceramic or glass fiber separators are often used with aqueous electrolytes. For best supercapacitor performance the separator should have a high electrical resistance, a high ionic conductance, and a low thickness (μm) [11].

Zirconium oxide, (ZrO_2), or zirconia, has several technological applications such as refractories, structural ceramics, biomaterials, oxygen sensors or fuel cell solid electrolytes, but was never used as a porous separator. Solid electrolytes based on zirconia generally have a thickness of 100-150 μm and exhibit a ionic conductivity over a wide temperature range (500 - 1000 °C) [36]. When heated up till its melting temperature, zirconia takes the form of one of its three polymorphs. Under normal conditions of temperature and pressure, it adopts the monoclinic structure or baddeleyite (m-ZrO_2). At approximately 1150 °C, zirconia is transformed into tetragonal zirconia with distorted fluorite structure (t-ZrO_2). Finally, at 2370 ° C it is transformed into cubic zirconia with fluorite structure (F-m-ZrO_2) [37][38]. These phase transformations are reversed in cooling, however, ceramics based on zirconia may be partially or totally stabilized by the incorporation of cations having valence numbers less than 4, such as Mg^{2+}, Ca^{2+}, Re^{3+} and Y^{3+} [38].

The most widely used oxide for partial or total stabilization of zirconia is yttrium oxide, Y_2O_3, which gives the ceramic a considerable increase in its electrical and mechanical properties. A Y_2O_3 content of 3 mol% leads to tetragonal zirconia (3YSZ). Doping with concentrations above 7% mol of yttria gives rise to cubic stabilized zirconia (CSZ) or yttria stabilized zirconia (7YSZ) and above 8% mol of Y_2O_3 content to fully stabilized zirconia (FSZ) or alternatively, yttria stabilized zirconia (8YSZ). Cubic stabilized zirconia has improved mechanical and thermal properties such as high strength, toughness, and thermal-shock resistance. The ionic conductivity of 8 mol% YSZ at 1000 ºC is of 0.18 Scm^{-1} [39]. The maximum conductivity for YSZ is obtained at ≈ 10 mol% Y_2O_3 content [27]. For Y_2O_3 content between those of tetragonal and cubic zirconia, a mixture of stable phases is obtained up to room temperature (RT) that it is known as partially stabilized zirconia (PSZ) [39]. Doping with 12 to 14 mol% Y_2O_3 content, generates oxygen voids that do not participate effectively in the conduction process, giving rise to more complex defects such as vacancy clusters or ordered impurity/vacuum pairs that hinder the mobility of cargo carriers. Even though the stabilization phenomena it is still not fully understood, it is known that it is influenced by the presence of anion vacancies, by the concentration and structure of the dopant and

by the electronic energy levels [38]. Oxygen voids are the predominant defects in solid solutions based on zirconia, particularly when zirconia is doped with trivalent oxides. Each added oxide molecule generates an oxygen vacancy, resulting in the concentration of vacancies being linearly dependent on the amount of dopant. Oxygen is transported by hopping through its vacancy sites by the vacancy diffusion mechanism and the formation of these vacancies is thermally activated [39].

3. MATERIALS AND METHODS

3.1. Equipment, materials, and reagents

For an easier reading, it was chosen to present the equipment, materials and reagents in comprehensive tables (equipment and material in Table 2 reagents in Table 3). Both tables present the name of the brand and for which purpose it was used. Table 2 also allows to understand in which step of the process the equipment was needed: if it was a general measurement, a process or characterization equipment. Materials and reagents are also separated depending on which component of the device it was used: electrode, separator or electrolyte.

Table 2 Name of the equipments, materials, correspondent brands and uses.

Name of the Equipment/Material	Brand	What it was used for
General Measurements		
Digital Scales	AND GR-200	3YSZ powder
	KERN Als	Graphite
	iBalance® i101™	Graphite
	Sartorios BP 110 S	3YSZ pellets open porosity
Digital Micrometer	Mitutoyo	3YSZ pellets thickness
Process		
Uniaxial Hydraulic Press	Specac	Making 3YSZ pellets
Turrax Mixer	IKA® Ultra turrax® Tubedrive control	Make PVA particles smaller
	IKA T10 basic Ultra-Turrax®	Mix binder with chemically exfoliated graphite
Muffle Oven	Ing.Climas Oven	Dry out the graphitic electrodes
Furnace	Nabertherm P330	Sinter 3YSZ pellets
Heating Plates	RS lab- 11C and P-Selecta®	Evaporate aqueous part of electrodes mixture
Micropipette (10:100µl)	Labnet Biopette^{PLUS}	
Ultrasonic Water Bath	Bandelin Sonorex Super RK 510H	Chemically exfoliate graphite
Regular 8'' sharpening stone	Gaoqiang Tools (importer: Jida Sociedade Unipessoal Lda)	Mechanically exfoliate graphite
Sharpening stone 10000 grit	(-)	Mechanically exfoliate graphite
Silicon Carbide Sandpaper (4000 grit)	Buheler	Mechanically exfoliate graphite
Electric Insulating tape	3M Temflex 1500 Vynil Plastic Electrical tape (100-260ºC)	Moulds (stacked tape)
Characterization		
X-Ray Diffraction System (XRD)	PANalytical XPert PRO	3YSZ and graphite samples
Raman Spectroscope	WITec alpha 300 RAS	Graphite/Graphene Samples
Potenciostat	Gamry Instruments Reference 3000 Potenciostat/Galvanostat/ZRA	Device performance
Four Point Probe System	Jandal Engineering LTD Leighton Buzzard Bedfordshire	Graphitic electrodes conductivity
Hall System	Nanometrics HL5500 Hall System	Determining Hall effect (mobility, majority carriers)

Table 3 Reagents

Reagent	Brand/Origin	Used for/to/as
Electrode (+)		
Block of electrographite	Electric furnaces of Siderurgia Nacional SA	Active material
Poly-vinylidene fluoride (PVDF)	Alfa Aesar Corp.	Binder
N,N-Dimethylfomammide (DMF)	Carlo Erba reagents	Solvent for PVDF
Acetone	LabChem	Chemically exfoliate graphite
Deionized water (milipor)		Chemically exfoliate graphite
Isopropyl Alcohol	LabChem	Chemically exfoliate graphite
Hydrogen Peroxide 30%	Carlo Erba reagents	Chemically exfoliate graphite
H_2O_2 (130 V) Hydrogen Peroxide 35%	LabChem	Chemically exfoliate graphite
Percarbonate	FULGOR™	Chemically exfoliate graphite
Electrode (-)		
Nickel	3801 Electrically Conductive Nickel Coating (Holland Shielding Systems)	Negative electrode
Separator		
3YSZ NPs 99.9% 30-50nm GNM	GNM-GETNANOMATERIALS	Separator
2-methoxyethanol	ROTH	3YSZ film
Poly(ethylene Glycol) (PEG)	Sigma-Aldrich	Binder for 3YSZ film
Poly(vynil alcohol) (PVA)	Sigma-Aldrich	Binder for 3YSZ film
Dichloromethane	Honeyell | Riedel-de-Haën™	PVA dispersant
Dioctyl sulfosuccinate sodium salt 96% (AOT)	Sigma-Aldrich	Surfactant for 3YSZ film
Deionized water (milipor)	(-)	Density measurement of 3YSZ pellets
Electrolytes		
KOH (6M)	Hidróxido de Potássio Lentilhas, LA (EKA - 101474)	Electrolyte
Sodium chloride NaCl (1M)	Sigma-Aldrich	Electrolyte
Na Cl brackish solution	Sigma-Aldrich	Electrolyte

3.2. Fabrication of porous Yttria-Stabilized Zirconia (YSZ) pellets

Considering that electrochemical supercapacitors have separators with porosities between 65-75% [10], it was attempted to achieve such porosity by making multiple experiments and using several methods. The first approach was to make a porous zirconia film through a solution-based method. Several polymers (PVA, PEG, PVDF) and surfactants (AOT) were used and even alcohol 2-methoxyethanol. This strategy led, every time, to non-homogenous cracked films, and was rapidly abandoned also because the samples resulted in ≈ 35% open porosity, a value that is significantly lower than what is needed. In a second approach, 3YSZ powder was compressed by hand in a square acrylic mold (laser-cut with 2.5 cm × 2.5 cm interior frame and without bottom) by using the acrylic piece (piston) that fit perfectly its frame. Several different bases were used.

The compressed 3YSZ nanopowder was sintered in its respective base. Idealy, this base should be smooth and without pores (so it would not stick to the film) and should resist high temperatures (>1450 ºC). Good fits could be tungsten, titanium or platinum, but they are very expensive and not readily available in the desired geometry. Some types of quartz and steel are also known to withstand high temperatures and were used as bases for the mold, but there was not specific information of the quartz and steel available at the laboratory that confirmed that the materials were in their pure form and/or were of a form that could withstand high temperatures. The first attempt using quartz (7 h ramp till 1450 ºC and 1450 ºC for 2 h) resulted in the diffusion of the 0.300 g of 3YSZ through the quartz, being all its surfaces covered with 3YSZ while the interior remained transparent, probably due to the immiscibility of both materials. A lower temperature was used (7 h ramp till 1300 ºC and 1300 ºC for 2 h) that resulted in the same output. When steel was used, it was possible to obtain a 3YSZ film, but the steel become brittle, contaminated the ceramic plate and in some places also stuck to the film. A block of electrographite was also used as a base and it was possible to obtain 3YSZ films, but the block

disintegrated, since this type of graphite was not of the refractory type. Also, the films obtained both with steel as a base or the graphite shrunk in ≈ 36% and had open porosities of ≈ 44%, which was still not sufficient. The need to make the process reproducible also meant that this approach had to be reconsidered.

The final attempt was to prepare 3YSZ pellets by cold uniaxial pressing and then sinter them using several sintering chronograms (from C1 to C8) as designated in Table 4. The mold used in the press was cylindrical with 5 mm radii, while the time under pressure was of ≈ 1 min. It should be noted that thickness control is defined by the pressure applied, but mainly limited by the amount of powder used. In this study amounts between 0.05 g and 0.2 g were used. For creating 3YSZ pellets with the desired porosity, thousands of samples were made, with and without add-ons, including liquid binders (such as PVA 5 % dissolved in water and PEG) and solid polymers (PVA, PVDF). For an easier understanding of the binder quantities, the measurements were made in µl per 0.1 gr of 3YSZ nanopowder. A more detailed and methodical study was made of the addition of solid particles of PVA, where its particle dimensions were reduced using Turrax® for 30 min at 4000 rpm. The calculus of the pellets' open porosity was obtained using the Archimedes Principle: they were submerged in distilled water, to simulate an aqueous electrolyte impregnating the open pores. Although not ideal, this is preferable to Helium pycnometry or other surface probing methods by gas adsorption.

Table 4 Sintering Chronograms for the 3YSZ pellets. R1: heating ramp 1 [ºC], R2: heating ramp 2 [ºC].

Designation	Polymer	R1 [°C /min]	$Temp_{R1}$ [ºC] / time [h]	Holding Temp. / Time - R1 [h]	R2 [°C /min]	$Temp_{R2}$ [ºC] / time [h]	Holding Temp. / Time –R2 [h]
C1	PVA	3.45	25 – 1450 / 7	1450 / 2	(-)	(-)	(-)
C2	PVA	3.1	25 - 1300 / 7	1300 / 2	(-)	(-)	(-)
C3	PVA	3	25 - 450 / 2.5	450 / 2	2.83	450 -1300 / 5	1300 / 2
C4	PVA	2	25 - 425 / 3.55	425 / 2	2.02	425 - 1300 / 7.23	1300 / 2
C5	PVA	2	25 - 425 / 3.55	425 / 2	1.8	425 - 1100 / 6.12	1100 / 2
C6	PVA	2	25 - 425 / 3.55	425 / 2	3	425 - 1000 / 3.20	1000 / 2
C7	PVDF	2	25 - 480 / 4	480 / 2	3	480 - 1100 / 3.45	1100 / 2
C8	PVDF	2	25 - 1100 / 9.17	1100 / 2	(-)	(-)	(-)

3.3. Exfoliation of graphite for the positive electrode

For the electrodes, a block of electrographite from was used as the active material. The electrographite was mechanically exfoliated with silicon carbide sandpaper 4000 grit, a common kitchen whetstone and a 10000 grit whetstone. The silicon carbide of the sandpaper reacted with some of the solvents used to try to exfoliate graphite. On the other hand, the 10000 grit whetstone did not yield enough powder in a reasonable amount of time. For these reasons, the graphite powder obtained with the common whetstone was used and subjected to different processing steps. The objective was to mix the graphite powder with solutions which might chemically exfoliate the graphite into graphene: isopropanol, hydrogen peroxide H_2O_2 (130 V), percarbonate and ultimately acetone and water. A block of electrographite was also subjected to temperature treatment (7 h ramp till 1300 °C and 2 h at 1300 °C). The presence of graphene in the powders was studied through the analysis of its Raman spectra.

The chemical exfoliation of graphite in acetone and deionized water (Millipore) is already studied in-depth in the paper of Yi et al [40], that studies graphene dispersions in these solvents. The proportions used are of 75 % of acetone to 25 % of water, with a particle concentration of 3 mg/ml. Several samples of this mixture were made. Some samples were subjected to sonication in an ice bath for 4 hours and the others for 6 hours [40]. The aqueous part of the mixture was then evaporated in a heating plate at 100 ºC. This method was used with the objective of obtaining the maximum percentage of graphene vs graphite in the final powder in a reasonable amount of time (tens of hours) using low-cost solvents. This method yielded a higher graphene to graphite ratio than the other ones, so the graphite powder obtained through this method was used as the active material in the prototyped device.

3.4. Nickel electrode

The commercial nickel aerosol, when dried, produces an electrical conductive film thanks to the air-drying acrylic resin in which the nickel is contained. It is generally used to prevent electrical interference which penetrates enclosures in insulating materials. The resin becomes touch dry 15 minutes after application and achieves maximum conductivity within 24 hours, preventing static build up. This aerosol has a volatile organic compounds (VOC) content in percent by weight of 61.4 % and a solid content of 38.6 %. It also presents a superficial resistivity of ≈ 0.5 Ω/ sq for a 50 µm thick film. In this case, it is used as negative electrode and presents other compounds that may interfere in the performance of the device. Table 5 presents the substances' amount in percentage ranges.

Table 5 Subtances present in the commercial nickel aerosol.

Substance name	Product identifier	%
Dimethyl ether	(CAS No.) 115-10-6 (EC No) 204-065-8 (EC Index) 603-019-00-8	25 - 50
Nickel powder	(CAS No.) 7440-02-0 (EC No) 231-111-4 (EC Index) 028-002-00-7	25 - 50
Xylene	CAS No.) 1330-20-7 (EC No) 215-535-7 (EC Index) 601-022-00-9	10 - 25
Toluene	(CAS No.) 108-88-3 (EC No) 203-625-9 (EC Index) 601-021-00-3	2,5 - 10
N-butyl acetate	(CAS No.) 123-86-4 (EC No) 204-658-1 (EC Index) 607-025-00-1	2,5 - 10
Acetone	(CAS No.) 67-64-1 (EC No) 200-662-2 (EC Index) 606-001-00-8	< 2,5
2-methoxy-1-methylethyl acetate	(CAS No.) 108-65-6 (EC No) 203-603-9 (EC Index) 607-195-00-7	< 2,5

3.5. Assembly and Characterization of the device

The binder used for the graphite powder was Poly-vinylidene fluoride (PVDF) dissolved in N,N-Dimethylfomammide (DMF) in a proportion of 1:10, mass to volume. A ratio 1:5 of graphite to binder was used. The mixture was homogenized with Turrax® for approximately 5 minutes. Firstly, electrodes were fabricated independently of the separator and their conductivity measurements taken. The solution was drop-casted into a hand-made square mold constituted by overlapping layers of insulating tape that were glued together to form a square-shape on an aluminum sheet. The electrodes were then dried at 60 °C for 16 h and cut through edges with a scalpel, so that the tape could be peeled off without damaging the electrode. Conductivity measurements were performed with the 4-probe method and the thickness of the samples measured with a digital micrometer.

A 3YSZ tablet with 48.67 % open porosity was used as the separator of the device. The electrode's paste was drop-casted on opposite sides of the tablet and left to dry at room temperature. Particularly, the commercial nickel aerosol used as the negative electrode was left to dry in a recipient, till a paste was formed. The total mass of the active material could be properly measured for the graphite electrode, but since nickel was obtained through a commercial source, it was not possible to determine the electrode's active material. Despite the error, it might be brought to the calculation, it was assumed the active material of the nickel electrode (effective mass of nickel) was the same as for the graphite electrode (0.013 g), with the total mass of the active material equaling 0.026 g, resulting in a device with a mass loading of 17 mg/cm^2 and a total weight of 0.355 g. In this case, although being a crucial component that constitutes an EES device (it is the greater contributor to the ESR) no special attention was given to the current collector, which was not deposited on the electrode. Here, performance

measurements were taken by confining the device in-between two glasses covered with conductive aluminum tape.

After the assembly of the electrodes on the separator, the electrolyte (KOH 6M)[2] was introduced laterally in the porous ceramic. The assembled device was then tested by Cyclic voltammetry (CV), Constant Current Charge-Discharge (CCCD) and Electrochemical Impedance Spectroscopy (EIS). As a side note, for an easier reading, the assembled Nickel - 3 Yttria Stabilized Zirconia - Graphite Electrical Energy Storage Device will be called, for simplicity, Ni@graphite device.

[2] 15.8 wt%

4. RESULTS AND DISCUSSION

4.1. 3YSZ separator

Using the press, although having removed the reproducibility issue and the “sticking” of the powder to the base, presented other challenges. The fact that the press did not allow the use of low pressures (like the ones used when the pressing was made by hand) and that the mold did not allow the entrance of air during the pressing process, led to highly dense pellets when only 3YSZ nanopowder was used. The vacuum created between the pistons didn’t allow to unstick the pellet between them until a threshold pressure was applied that allowed for the total removal of the air in-between the particles of the powder being compressed, which led to super dense pellets. Besides wanting high porosity, another main condition was to fabricate a porous 3YSZ separator that kept its physical integrity, so it could be handled manually, before and after sintering. Only 2 out of 10 pellets generated (0.1 g of 3YSZ nanopowder subjected to 1.5 kgF) were crack-free and could be sintered. After sintering the ill-distributed tensions in the compressed nanopowder resulted in highly dense and deformed pellets. Pellets of 0.2 g of nanopowder and 2.5 kgF applied were easy to compress without deformation, but were also highly packed: open porosities were close to zero in both cases. When working only with the nanopowder (0.5-1.5 g) it was also observed that high pressures (7-11 kgF), for the amounts used, would always resulted in cracked samples.

The main problem encountered with solution-based polymers was the difficulty to uniformly distribute the solution in the minimal quantity of 3YSZ nanopowder. The non-homogeneity of the viscous liquid through the powder also led to cracked pellets before and after the sintering process. Another requirement for the pellets is that they can be easily removed from the mold, so the powder should not stick to it. For that to happen, the quantity must be enough to still have a loose powder, what was deemed insufficient for having the desired porosity. This was proved experimentally by using PEG. Only 5 out of 20 samples could be sintered, cracked after sintering (0.15 g 3YSZ; 4.5-5µl/0.1 g PEG; 4-5 kgF;) and had negligible porosity. The rest of the samples never reached the sintering part of the process since they disintegrated in the press: for 0.1 g of powder, 5 to 7.5 µl/0.1 g of PEG was used and 3 - 4 KgF was applied; for the 0.2 gr samples 5 -15 µl/0.1 g of PEG was used and 4 - 7 KgF was applied. The same experiments were made with PVA 5 % (dissolved in water): 0.2 g of nanopowder was used, 7.5-12.5 µl/ 0.1 g. Only this time dichloromethane was added in a proportion of 5 ml per 0.1 g of nanopowder and the mixture left to dry. Dichloromethane was used as a dispersant of the polymer, with the intent of homogenize the polymer in the powder. The dried powder was the subjected to 5kg. Of the 4 samples made, one presented transparent stains, two were totally white and the other cracked. This method was not pursued further.

After several trials, the solution found to control the porosity of 3YSZ pellets was to add solid PVA particles to the 3YSZ powder in several proportions. Three standard quantities of nanopowder were used as a reference: 0.1 g, 0.15 g and 0.2 g. The 3YSZ:PVA ratio studied were 1:1; 2:1; 3:1; 3.5:1; 4:1; 5:1; 6:1; 7:1. From the samples of ratio 1:1 to 3:1, where the force applied ranged between 1 and 11 kgF, it was observed that pressures superior to 5 kgF generally led to a greater percentage of cracked pellets after the sintering process. For this reason, for the remaining samples (4:1 to 7:1), forces between 1 - 5 kgF were used in the tests and 0.2 g of 3YSZ nanopowder were used from then on, in every sample. Ratios above 4:1 (5:1; 6:1; 7:1), where the chronogram 4 was used, revealed ever-decreasing percentages of open porosities, 27.3 %, 23.6 % and 23 % respectively.

The proportion YSZ:PVA that presented higher open porosities with chronogram 4 (C4) was the ratio 4:1, with 36 % of open porosity. With this ratio, different sintering chronograms where used, mainly with less steeper rates and lower peak temperatures: with chronogram 5 (C5) open porosities of 49.5 % were attained and with chronogram 6 (C6), 55.6%, with an average thickness of 863.5 µm. However, samples obtained with C6 were bumpy and fragile, not ideal to use in a prototyped device. It was considered then, that the limit of porosity with this particle-size of PVA was attained. Since there was no form of reducing even more its size, a polymer that commercially had a smaller particle-size was used: PVDF. Ratios of 3YSZ:PVDF of 2:1 and 2:1.5 were studied, where chronogram 7 (C7) and chronogram 8 (C8) were used, respectively, resulting in smooth, defect-free pellets. Ratio 2:1 and 2:1.5 attained porosities of 52.7 and 59%.

Although the separator thickness is significantly higher than it is supposed to, its effective thickness after the deposition of the electrodes by casting is significantly lower, since the electrodes' paste diffuses through the open pores at the surface of the separator, augmenting the surface-area.

4.2. Phase Identification of the separator by XRD

The 3YSZ nanopowder was analyzed through XRD, to identify the phases of the crystalline structure before the sintering process. The spectrum peaks matched with two other spectra, corresponding to monoclinic (37%) and tetragonal (63%) phases.

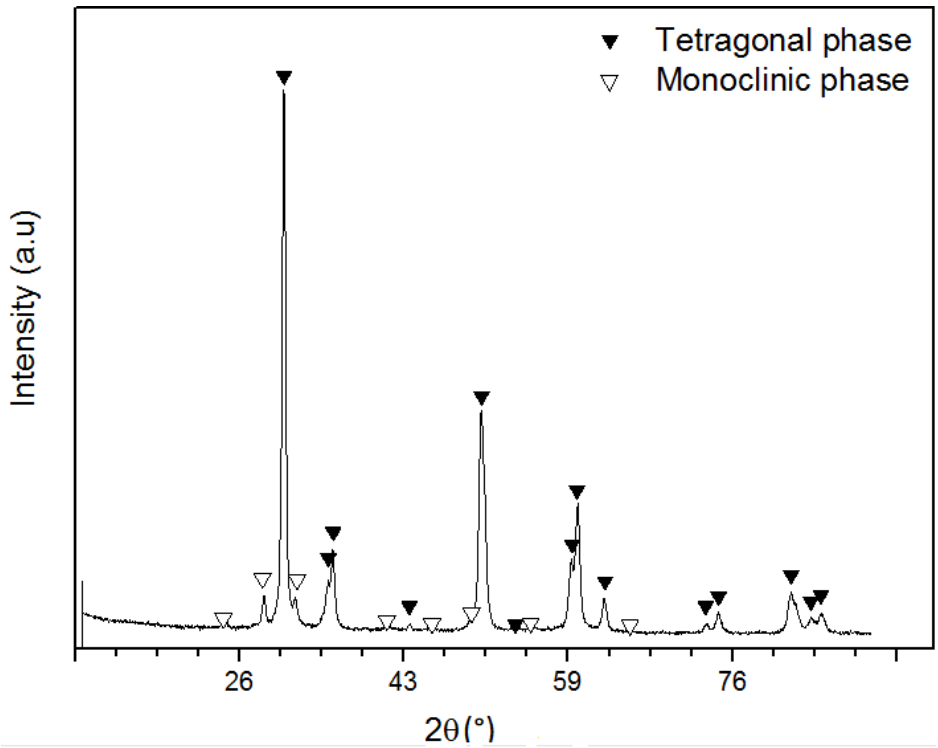

Figure 3 XRD spectrum of Comercial zirconia

4.3. Raman Characterization of exfoliated graphite

Raman spectra was used to identify the presence of graphene in exfoliated graphite. In graphene, the Stokes phonon energy shift caused by laser excitation creates two main peaks in the Raman spectrum (G and 2D) and one smaller peak, D (1350 cm^{-1}) that may be apparent when defects within the carbon lattice are present. D and 2D bands are dispersive, which means that there are a number of very weak modes underlying these bands that will be enhanced (position and shape will vary) depending on which excitation laser is used. It is important to use the same excitation laser frequency for all measurements while doing characterization with the D band [41], so 532 nm laser-frequency was used for all samples. In Table 6, the positions of G a 2D peaks of all samples are listed. Each sample is identified by a short name, with which it will be referred in the future.

The 2D band (peak at 2690 cm^{-1}) is always a strong band in graphene and its used to determine graphene layer thickness of less than 4 layers, depending on both position and band shape. For single layer graphene, the 2D band is observed to be a single symmetric peak with a full width at half maximum (FWHM) of ≈ 30 cm^{-1}. Adding successive layers of graphene causes the 2D band to split into several overlapping modes due to the symmetry lowering [41]; these modes combine to give a wider, shorter, and higher frequency peak [42], as it occurs for all samples referred in Table 6. It should be noted that the value of FWHM, is for all samples, invariably higher than the double of what it should be for single layer graphene, reaching its higher value for G*Exf.

Table 6 G and 2D peak positions (Xc), FWHM of D band respective standart deviations (%) in [cm^{-1}].

Long Name	Short name	G	2D	FWHM(2D)
Theoretical Xc (graphene) [41]		1580	2690	30
Grinded* (common)	G*	1572 ± 3.8	2683 ± 5.9	77 ± 2.3
Grinded 4000 grit (SiC sandpaper)	G4000	1564 ± 0.2	2672 ± 0.5	80 ± 1.0
Grinded 10000 grit	G10000	1582 ± 0.3	2704 ± 0.7	73 ± 2.4
Grinded* + Isopropanol	G*Iso	1573 ± 2.9	2685 ± 4.0	77 ± 2.2
Grinded* + Peroxide	G*Perox	1582 ± 0.2	2708 ± 0.8	69 ± 1.6
***Grinded* + H_2O_2 (130 V)**	G*130V	1581 ± 0.3	2700 ± 0.5	74
Grinded* + Percarbonate	G*Per	1581 ± 0.2	2704 ± 0.7	74
Block 1300 °C	B1300	1580 ± 0.2	2706 ± 0.9	66 ± 3.1
Grinded* + Acetone + water	G*Exf	1566 ± 0.2	2678 ± 0.5	81 ± 1.3

In some of the samples of Table 6, it is possible to observe redshifts or blueshifts of G and 2D peaks when comparing its positions with the theoretical positions of the graphene spectrum [41]. A redshift in the G peak, is related to an increasing number of layers [42]. G4000 and G*Exf present the biggest redshifts. On average B1300 presents a peak position closer to that of graphene.

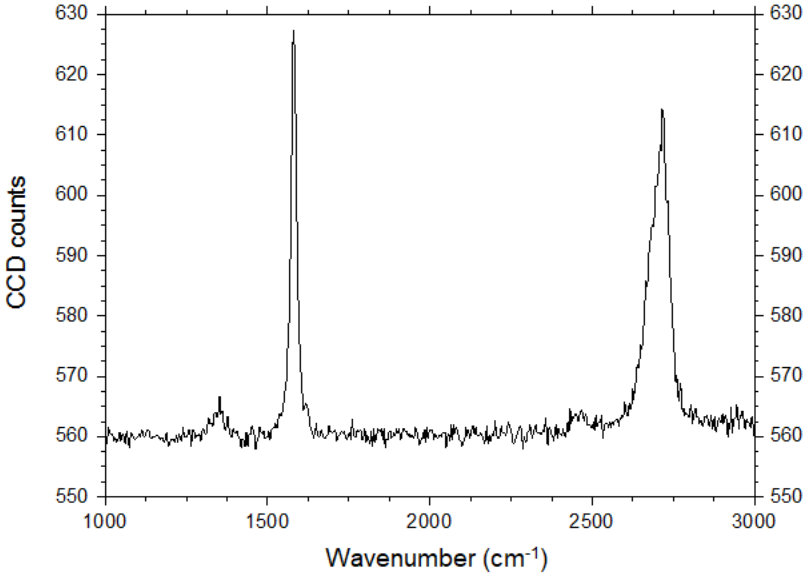

Figure 4 Raman spectrum of one of the datapoins of Block 1300, with a I_{2D}/I_G ratio of 0.97.

The intensity of this G band (peak at 1580 cm^{-1}) closely follows a linear trend as the sample progresses from single to multilayer graphene, so it can be used to determine graphene thickness. Number of layers is given by *n* in Equation 1

$$\omega_G = 1581.6 + 11/(1 + n^{1.6}) \qquad \text{Equation 1}$$

where ω_G is the band position in wavenumbers [42]. According to the literature, this method is the least susceptible to the effects of strain, temperature and doping. However, Equation 1 alone was not useful to determine the number of layers present in the samples: with respect to the peak position all resulted in *n=1.* The number of layers can also be estimated from the ratio of peak intensities of 2D and G peaks, I_{2D}/I_G, that for high quality (defect free) single layer graphene it should equal 2. This ratio, lack of a D band and a sharp symmetric 2D is often used as a confirmation for a high quality defect free graphene sample [41]. In Table 7 it can be observed this is not the case for the presented samples. It should be noted that G*Exf is the sample that, according with the ratio I_{2D}/I_G, possesses the higher quantities of graphene, although a ratio of 0.9 is still far from the ideal 2. Nevertheless, Block 1300

presents the higher ratio I_{2D}/I_G =0.97 for one of its data points, as seen in Figure 4, a value that, although not representative, it is the most approximate to that of single-layer graphene [41].

Table 7 I_{2D}/I_G and I_D/I_G ratios obtained from the Raman spectra of the samples obtained at a laser excitation of 532nm.

Long Name	Short name	I_{2D}/I_G	I_D/I_G	D peak intensity
Grinded* (common)	G*	0.51	0.49	636.19
Grinded 4000 grit (SiC sandpaper)	G4000	0.41	0.34	795.00
Grinded 10000 grit	G10000	0.86	0.86	583.54
Grinded*+ Isopropanol	G*Iso	0.62	0.52	655.72
Grinded*+ Peroxide[3]	G*Perox	0.60	0.52	638.30
Grinded*+ H_2O_2 (130 V)	G*130V	0.57	0.53	716.15
Grinded*+ Percarbonate	G*Per	0.79	0.76	580.68
Block 1300 °C	B1300	0.67	0.48	519.14
Grinded*+ Acetone + water	G*Exf	0.90	0.85	568.46

Using the ratio of peak intensities I_D/I_G, one can use Raman spectra to characterize the level of disorder in graphene. Average values of the I_D/I_G ratios and D peak intensities obtained from samples' Raman spectra are presented in Table 7. As disorder in graphene increases, I_D/I_G displays two different regimens, one with low defect density called the "Nanocrystalline graphite phase" (D peak is week) and high defect density or "Mainly sp^2 amorphous carbon phase" which enhances the D peak strongly (I_D/I_G will begin to decrease as an increasing defect density results in a more amorphous carbon structure, attenuating all Raman peaks). Graphene is considered to be in the nanocrystalline graphite regimen [42]. All Raman spectra obtained presented D peaks (except in rare cases) with varying intensities. In particular, G*Exf presented other peaks that could not be identified between 500-1000 cm^{-1}, which are probably due to contamination. These are shown in Figure 5.

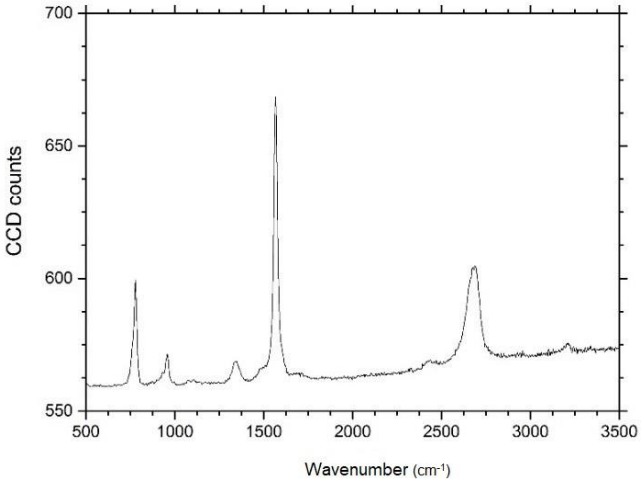

Figure 5 Raman spectrum of sample G*Exf

4.4. Conductivity of graphite electrodes

The conductivities of the dried electrodes were obtained through the 4-point probe method, where a current is injected through the probes and the tension values are measured. Currents between 1-10 mA

[3] The maximum cell voltage is essentially limited by the positive electrode. When the maximum potential of the positive electrode is too high, it will lead to irreversible electro-oxidation on the active sites of the carbon electrode. It could be pushed to slightly lower values through controlled chemical oxidation of carbon with hydrogen peroxide, allowing the maximum voltage to be slightly increased with an excellent stability [9].

and the respective symmetric values were used to calculate the conductivity, resulting in 20 measurements for each sample. Depending on the thickness (t) of the samples either of two equations are applied to know the values of resistivity. Knowing that *s* is the probe spacing (1 mm in this case) and since the mean thickness of all samples is 0.238 ± 0.05 mm, the condition $t/s \ll 1$ is verified and Equation 3 applies for the calculation of resistivity of all samples.

$$\rho = 2\pi s \frac{V}{I} \qquad \text{Equation 2}$$

$$\rho = \frac{\pi}{\ln(2)} t \frac{V}{I} = 4.532 t \frac{V}{I} \qquad \text{Equation 3}$$

Being the conductivity the inverse of the resistivity, average of the conductivity values obtained for exfoliated graphite (4h sonication, PVDF as a binder) was of $(1.17 \pm 0.18) \times 10^3$ S/m, for a percentage of active material of 27.93 %, which has the same order of magnitude of the values in the literature for compacted graphite at high pressures (5 MPa) [34], with the exception that these electrodes were not subjected to a calendaring process (electrode compaction) and despite that, reached similar results. This is due to the process of chemical exfoliation that yielded a certain percentage of graphene. Nevertheless, a packed powder difficultly reaches conductivities of the bulk material it was made of [34], that for graphite is in the range of 10^4 S/m at room temperature [43]. In this exfoliated graphite, the majority carriers were determined to be electrons with a concentration of - $5.22 \cdot 10^{17}$ cm^{-2} (correspondent to a sheet resistance of 6.013 Ω/sq.) and with a mobility of 1.98 $cm^2/V \cdot s$. Considering the addition of an insulating binder it is normal that does not reach the off-plane mobility of graphite of 35 $cm^2/V \cdot s$ [44].

4.5. Characterization guidelines for evaluating performance of the device

The performance of a supercapacitor can be characterized by a series of key parameters, including cell capacitance (C_T), operating voltage, (V_0), Equivalent Series Resistance (ESR), power density (P_D), energy density (E_D) and time constant (τ). To accurately measure these parameters, a variety of methods have been proposed and are used in academia and industry. As a result, some confusion has been caused due to the inconsistencies between different evaluation methods and practices. Such confusion hinders effective communication of new research findings, and creates a hurdle in transferring novel supercapacitor technologies from research labs to commercial applications. To evaluate supercapacitors performance, three essential parameters, C_T, V_o, and ESR, are often used to assess their energy and power performance, and usually are sufficient for commercial products where the materials, fabrication, and cell design are all fixed [1].

Various instruments or test modes have been developed and applied to characterize the electrochemical performance of supercapacitors. Cyclic voltammetry (CV), Constant Current Charge-Discharge (CCCD) and Electrochemical Impedance Spectroscopy (EIS) tests are commonly used. In essence, all such instruments can be used to measure the three fundamental parameters: voltage, current and time; all the other can be derived from them. However, each of the instruments has its own focus and targeted parameters, by design. However, the most effective and accurate approach is CCCD testing to measure the three essential parameters (C_T, V_o, and ESR). Subsequently, the time constant, energy and power densities, and leakage and maximum current of supercapacitor devices can be derived from these three core parameters [6]. It is worth noting that the capacitance values measured for a range of porous carbons can vary substantially with discharge current due to a greater possibility of restricted electrolyte diffusion in narrower pores. Ideally, reported capacitance values of carbon electrodes, particularly when used for comparative purposes, should be measured and compared at a fixed current density [2].

4.6. Cyclic Voltammetry: Identifying charge storage mechanism

Cyclic Voltammetry (CV) is a technique where the potential at the working electrode is swept back and forth (linear scanning) across a given potential window at a constant rate, giving Current vs Potential plots. The resulting current is measured and plotted against the potential [45]. The CV is very useful for

evaluation of capacitive behavior of a device or electrode made from a synthetic pure or composite material [8]. Through the integration of the resulting cyclic voltammograms, the accumulated charge as a function of potential can be obtained. Then, the capacitance can be estimated as the total charge divided by the "potential window"[4], as depicted in Equation 4 [46]

$$C_T = \frac{\Delta Q}{\Delta V} \qquad \text{Equation 4}$$

CV was performed of the Ni@graphite device at scan rates of 10, 50 and 100 mV/s. The shape of CV was compared with typical EES devices, presenting similar curves to the ones of EDLC and Pseudocapacitors, that for ideal constant capacitance, are characterized by having classic rectangular cyclic voltammograms, as depicted in Fig 6 [4].

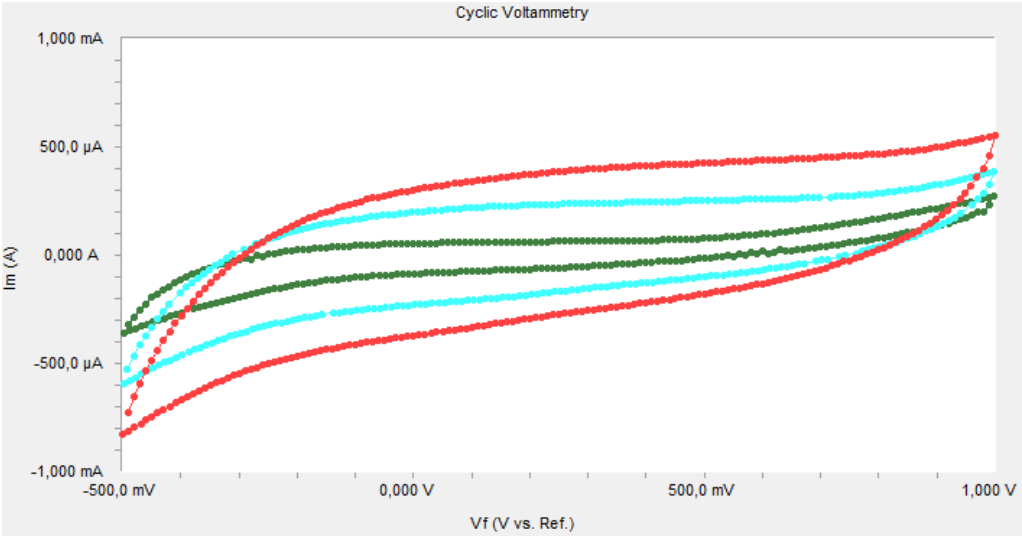

Figure 6 Cyclic Voltammetry of Ni@graphite EES device. Each curve representing Curve 4 of 5 cycle curves made with each scan rate: 100 mv/s (red), 50mV/s (blue), 10 mV/s (green).

The capacitance was calculated using Equation 4, dividing the charge obtained by integration of the cyclic voltammograms by the potential window used (1.5 V). Its values are shown in Table 8. Specific capacitance of a EC is the capacitance per unit mass for one electrode (F g^{-1}) [2],[47]. The specific capacitance (C_S) of a full cell or single electrode can be determined by the I-Vf CV plot through the following relation:

$$C_{SP} = \frac{4C}{\Pi} \qquad \text{Equation 5}$$

where C is the measured capacitance for the two-electrode cell and Π stands for the normalization by mass, area, volume etc. Specific capacitance values (in units of F/g, F/cm^3, or F/cm^2) obtained from the two-electrode system will typically be on the order of 4 times smaller than for the three-electrode, half-cell system [45]. The multiplier of 4 adjusts the capacitance of the cell and the combined mass of two electrodes to the capacitance and mass of a single electrode [3], [47], [48]. Values of specific capacitance are presented in Table 8, according with this equation, normalized both by the mass (total active material and total mass) and area.

Variations in electrolyte–electrode surface interactions that arise from differing electrolyte properties (viscosity, dielectric constant, dipole moment) will also influence wettability and, hence, electrolyte penetration into pores. It should be noted that at low charge rates or frequencies, electrolyte ions have time to penetrate the depth of the pores and additional surface-area is accessed (and distributed

[4] Normally, the whole curve is recommended to for use. However, in practice, different segments of the curve have been used in integration, thus leading to inconsistencies in test results [6]

resistance is also at a maximum). As the charge rate or frequency increases, electrolyte penetration becomes poorer and less surface-area is accessed. Similarly, larger pores lead to a lower distributed electrolyte resistance and greater electrolyte penetration that enables most of the surface-area and hence the capacitance, to be utilized [2]. This explains why the values of capacitance in Table 8 increase with lower scan rates.

Operating voltage is also an important determinant of both the energy and the power of supercapacitors (both are proportional to V_0^2) and its dependent on electrolyte stability [2], [11]. Both CV and CCCD tests can be used to determine V_0 of either the supercapacitor materials or the devices. However actual testing of this maximum potential carries the risk of destroying the cell. An expedient method is usually applied, V_0 can be achieved by starting with a lower voltage applied to the cell and then slowly increasing the voltage until a spike appears at the boundary of the potential window. These spikes can be observed in Fig. 6, determining an operation voltage of 1.5 V. The other factor influencing V_0 is the cell configuration. In an asymmetric system, V_0 can be increased by using different supercapacitor materials so, as to introduce additional electrochemical potential difference. This way, even in aqueous systems, V_0 can reach 2.0 – 2.3 V, giving rise to much improved energy storage [6].

Table 8 Charge, Q, (mC), Capacitance (mF) and Specific Cpacitance (Fg^{-1}) of the average of Curve 3,4 and 5 at different scan rates in mV/s.

Scan rate [mV/s]	Q [mC]	C [mF]	Cs [Fg^{-1}] active material	Cs [Fg^{-1}] total mass	Cs (Fcm^{-2})
10	9.46 ± 0.11	6.31 ± 0.07	0.97 ± 0.01	0.071	0.032
50	5.29 ± 0.11	3.53	0.54	0.039	0.018
100	4.22	2.35	0.36	0.027	0.012 00

The current flowing through a capacitor is in a linear relationship with the sweep rate (or scan rate), v, but independent of voltage. Here, the current, I, not only increases proportionally with the increase of v, but also follows the direction of voltage variation, i.e. v is positive when voltage increases and it is negative when voltage decreases [8]. The current response to an applied sweep rate is different, depending on whether the redox reaction is surface-controlled (capacitive) or diffusion-controlled (faradaic). For a capacitive process, the instantaneous current induced by the EDL mechanism is proportional to the scan rate, v [4], [6], [17]. Of the three pseudocapacitive mechanisms (intercalation, redox and underpotential pseudocapacitance), underpotential deposition and surface redox reaction pseudocapacitance exhibit kinetics indicative of surface-controlled electro-chemical processes, that is, all three mechanisms happen roughly on the same time scale and are capacitive in nature. This means that in experimental terms, both types of pseudocapacitance exhibit rectangular cyclic voltammograms and for that reason, also verify a proportional relationship between current and scan rate [6], [8], [43].

For a redox reaction limited by semi-infinite diffusion the peak current I is proportional to the square root of the scan rate (as $v^{1/2}$) [6] and so does intercalation pseudocapacitance. In intercalation pseudocapacitance charge storage does not occur on the surface, but in the bulk material, although the kinetics are limited by surface processes (it is not diffusion-limited) so that the overall behaviour seems capacitive. Intercalation pseudocapacitance is rarely observed because in most intercalation materials charge storage (even in thin films) is limited by solid-state diffusion and therefore the peak currents scale with $v^{1/2}$. The relationship of both mechanisms can be expressed by Equation 6

$$i(V) = k_1 v^{1/2} + k_2 v^1 \qquad \text{Equation 6}$$

where ν is scan rate (mV/s). Calculating the values of k_1 and k_2 at each potential will give the contribution of each process. Here, k_1 reflects the sum of redox reactions and intercalation pseudocapacitance contributions, while k_2 reflects the sum of of capacitive, redox pseudocapacitance and unperpotential pseudocapacitance contributions. Through the cyclic voltammograms, current values for the same voltage were taken at different scan rates and a graphic current vs scan rate was plotted (Fig. 7). The fitting of the curve was made using Equation 6. The value obtained for k_1 was of $1.55 \times 10^{-5} \pm 2.54 \times 10^{-6}$ and for k_2 of $1.51 \times 10^{-6} \pm 2.87 \times 10^{-7}$. Considering that the CV curves obtained for the Ni@graphite device do not present redox peaks at the lowest scan rate (10 mV), we can either presume those peaks could have being revealed at even lower scan rates (e.g. 0.1 mV/s) or assume that the value of k_1 is

entirely due to intercalation pseudocapacitance. and that, surprisingly, this is the prevalent charge storage mechanism.

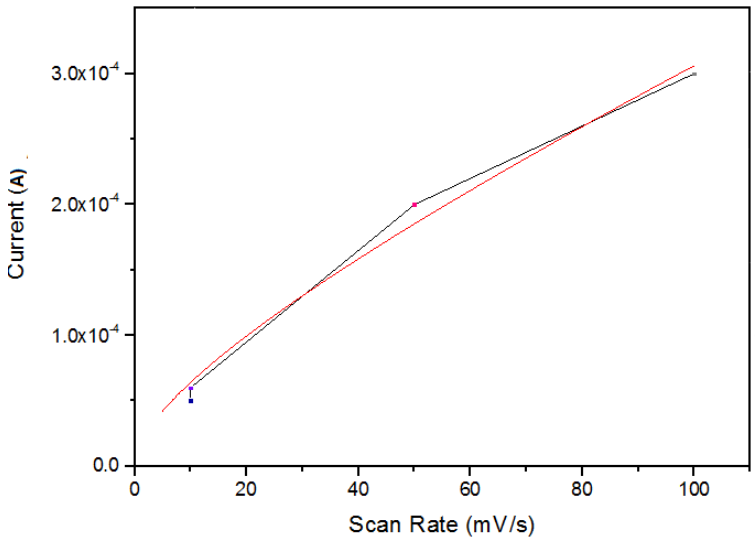

Figure 7 Relationship betwen scan rate and capacitance with $i = 1.55\times10^{-5}\ v^{1/2} + 1.51\times10^{-6}\ x$ and $i_{error} = 2.54\times10^{-6}\ v^{1/2} + 2.87\times10^{-7}\ v$

4.7. Constant Current Charge-Discharge (CCCD)

In the galvanostatic charge-discharge curves, the pseudocapacitive process without phase change is indicated by a linear-shaped profile of potential *vs.* capacity. In addition, the voltage hysteresis between the charging and discharging steps is very small. These characteristics are different from those of batteries, which manifest an obvious voltage plateau in charge-discharge curves [17]. Five cycles of CCCD were performed at a constant current of 1.13×10^{-5} A, with charge and discharge times of 5 and 10 min respectively, as shown in Fig.8.

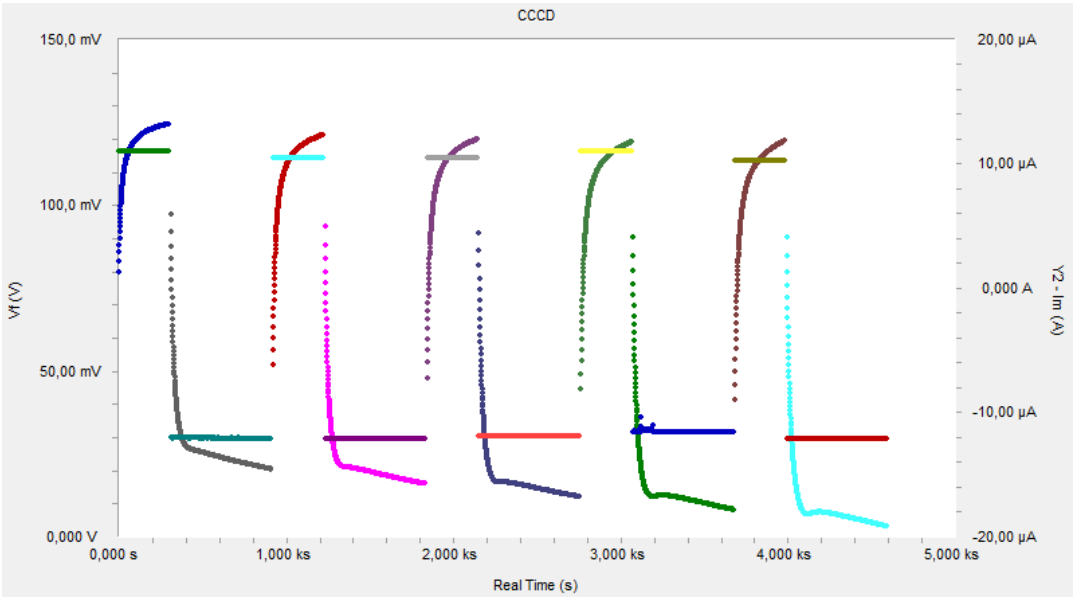

Figure 8 Constant Current Charge Discharge (CCCD) test of the Ni@graphite device.

The stored electric energy can be obtained from the charging curve (by integration of the charging curve one can obtain the capacitance, presented in Table 10, and the deliverable energy from the discharging curve [6]. In addition, in CCCD curves, there are usually a drop in potential between the end of charge and the beginning of discharge that is denominated Internal Resistance drop (IR drop), which originates from the change of internal resistance, including the resistance of the electrolyte, electrode materials and other connectors or auxiliaries [29]. Applying ohm's law to the IR drop allows to determine the ESR in supercapacitors. The accuracy of the calculated ESR can be affected by the dwelling time and size of supercapacitor [5] (in this case a dwelling time of 10 seconds was used), however, the curves presented are either that of an hybrid [6], an EDLC or a PC [15] [45], not even of a rechargeable battery [56] [29]. These curves are similar in shape to RC curves of a capacitor, but present high non-linearity. As can be observed by the graphic, the charging and discharging time are not symmetric, since the discharging is made in a few seconds and then it reaches a plateau. This high non-linearity prevents accurate measure of ESR, capacitance or deliverable energy.

4.8. Constant Current Discharge

Galvanostatic or constant current discharge is the accepted measurement method for determining capacitance for packaged ultracapacitors in the ultracapacitor industry and correlates more closely to

[5] CCCD test is usually carried out without dwelling at the peak potential, that is, the discharging starts once the peak potential is reached. However, the practice of non-zero dwelling time is widely adopted in tests, which can greatly influence the final value of ESR. A couple of different dwelling times have been reported varying from 0–30 min [6]. A larger charge/discharge current used in the test will usually give rise to a smaller R_{ES}, so for comparison purposes ESR of different device should be compared at the same current [33] [45].

how a load is typically applied to an ultracapacitor in most of applications [47]. Cell capacitance can then be determined by Equation 7,

$$C = \frac{I}{dV/dt} \qquad \text{Equation 7}$$

where *I* is the discharge current and dV/dt is calculated from the slope of the CC discharge curve. The discharge curve obtained for the Ni@graphite device is plotted in Fig.9, where for a constant current of 1×10^{-5} A, the resulting capacitance obtained by Gamry Echem Analyst is of 25.84 mF, which gives us a specific capacitance (considering the active material) of 0.99 Fg^{-1}. Capacity (A-h) can also be calculated through the discharge curve by having in consideration the current used for discharge (I = 1×10^{-5}) and the time of discharge (2443 s instead of 3600s, as determined by the capacity's definition). The value of the capacity calculated was of 6.78 µA-h, which is in accordance with the value obtained through Echem Analyst.

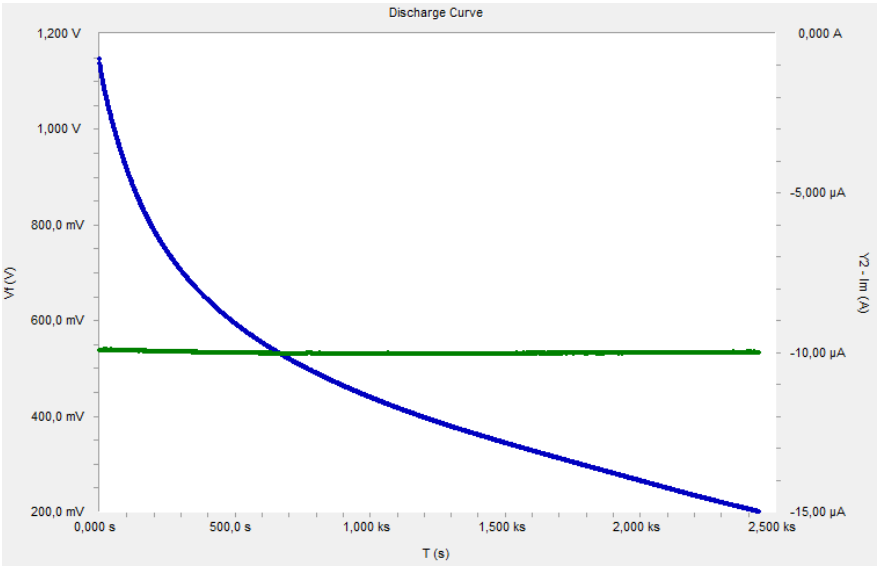

Figure 9 Discharge curve of Ni@graphite device.

Time constant[6] of the device, defined as the product of ESR and C_T, as shown in Equation 8 [33],

$$\tau = R_{ES}C_T \qquad \text{Equation 8}$$

can only be determined by self-discharge of the device and not for a controlled discharge at constant current as performed here. The self-discharge current time dependence can be fitted by Equation 9 in a conventional capacitor. Nevertheless, self-discharge of the device was not performed [7], without which it is impossible to obtain ESR through the time constant and consequently maximum power, leakage current, $I_{leakage}$, and maximum current $I_{máx.}$

$$V(t) = V_0 e^{(--\frac{t}{\tau})} \qquad \text{Equation 9}$$

The leakage current is widely used in industry to evaluate the capability of a supercapacitor to maintain the rated potential when not in use. Normally, it is recorded as the compensating current that is applied to hold a fully charged device after 72 h. Maximum peak current, which usually appears in the

[6] A smaller τ reflects better responsiveness of the device, and for most of commercial supercapacitors, τ normally ranges from 0.5 to 3.6 s.Normally τ is fixed around a certain value for supercapacitors produced using the same technology [33].

[7] Due to time and equipment limitations.

specifications for commercial supercapacitors. It is evaluated by discharging a fully charged SC device from V to ½ Vo in 1 s, and calculated as in Equation 10 [33].

$$I_{máx} = \frac{E}{\tau+1} \qquad \text{Equation 10}$$

4.9. Electrochemical Impedance Spectroscopy (EIS)

Potenciostatic Electrochemical Impedance Spectroscopy (EIS) was carried out to further explore the electrochemical behaviors of the Ni@graphite device. EIS measures the impedance as a function of frequency by applying a low-amplitude alternative voltage (normally 5 mV) superimposed on a steady-state potential. The resulting data is usually expressed graphically in a Bode plot, to demonstrate the cell response between the phase angle and frequency, and in a Nyquist plot, to show the imaginary and real parts of the cell impedances on a complex plane [6]. In this case AC voltage used was of 50, 100 and 500 mV rms. Modeling of data using an Electrical Equivalent Circuit (EEC) was conducted using the Model Editor of Gamry Echem Analyst to extract quantitative information about the processes occurring at the electrode's surface. Typically, the fit between the model circuit and the Nyquist plot is examined to determine if the circuit is a good model for the system. Nevertheless, each component of the circuit model represents a different electrical phenomenon, thus, a simple comparison of the Nyquist plot is not sufficient to elucidate the best model for the system [49], since there could be a model that allows a good fit but that doesn't actually represent the phenomena occurring in the device.

Electrical Equivalent Circuit and Fractional Residual Errors

Many EECs have been used in the literature to model supercapacitors, however, the most common is the modified Randles Circuit, that models the situation of an electrode in contact with an electrolyte [50] and that was also used to model this device. The EEC that best fitted the Nyquist Plot of the Ni @graphite device is represented below (Fig. 10), and it can be divided in four blocks, each one representing a physicochemical phenomenon in the cell. The first one, starting from the left, includes the contact resistance of the electrode with the current collector ($R_{contact}$) and an induced impedance (L_{gamry}) related with the measuring device, that although represented (because it allowed a better fit) it is not actually an element that models something in the device itself. The second block is constituted by three elements in parallel: a Constant Phase Element (CPE)[8] that represent double-layer capacitance (C_{dl})[9], the charge transfer resistance (R_{ct}), also called polarization resistance (R_p)[10], which models the faradic charge transfer reaction at the electrode surface[11] and an inductance associated with high concentration of electrolyte (KOH 6M) at AC frequencies, which is rarely represented in most models [51]. The third block is formed by the interfacial capacitance ($C_{inteface}$) and surface-layer resistance (R_{sl}), while the final block represents the capacitance associated with ion diffusion, that although related with Warburg impedance, that model linear diffusion toward the electrode surface, it is better represented by a CPE element. All these blocks, of course, are connected in both extremes to the reference electrode (R.E) that is the carbon-based electrode (exfoliated graphite) and the Working electrode (Nickel). The values obtained for the model's parameters are also exhibited in Fig 10, where the EEC is schematized and in Table 9.

[8] The CPE accounts for inhomogeneities at the surface of the electrode and is generally used to simulate non-ideal capacitors and it is associated with pseudocapacitive behavior, also called semi-infinite diffusion [17]. To be thorough, the experimental data must be modelled with and without the CPE to determine which circuit provides a better fit of the data [51].

[9] Double-layer capacitance measurements can provide information on adsorption and desorption phenomena. In some systems, a C_{DL} measurement may not represent the double layer capacitance. Rather, it may indicate the degree of film formation or the integrity of an organic coating [55].

[10] In the simple cases, the polarization resistance and the charge transfer resistances are identical. However, for more complicated cases they may not be equal. For both types of resistance, you must subtract the solution resistance to get an accurate value [55].

[11] which can be reversible or irreversible.

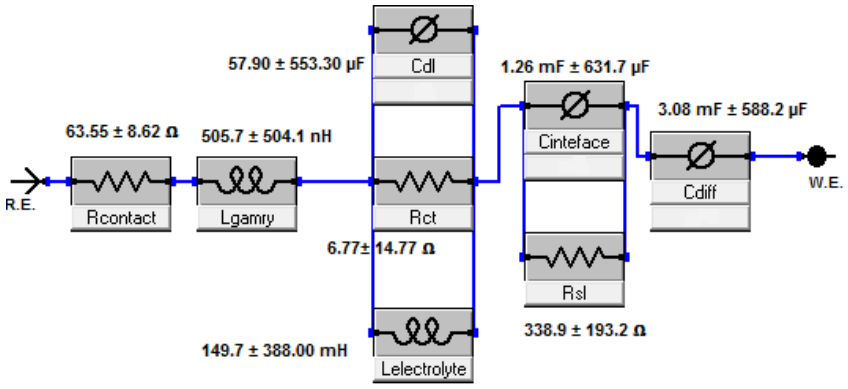

Figure 10 EEC of Ni @graphite

The values obtained for some elements of the model present substancial error (higher than the actual measure) despite the good fit. In a first instance a possible explanation would be the situation of over-fitting, where there are elements present that don't have physical manifestation, but a probably better hypothesis is that EEC model used is not adequate. Models based on the Randles Cell are good for approximations and for describing electrochemical interfaces of planar electrodes, but they describe poorly the interaction of electrolyte ions inside the pores of the carbon (or other) electrodes that are used in most electrochemical cells [52], as is the case for the graphite electrode in this device. In supercapacitors based on porous electrodes, an Equivalent Distributed Resistance (EDR) arises that is due to electrolyte resistance that extends into the depth of the pore. This resistance is coupled with distributed interfacial capacitance elements and leads to an electrode with a non-uniform distribution of effective resistance and capacitance (commonly referred to as the 'transmission line model'). A distributed RC network then arises that restricts the rate of charge and discharge. This situation has also been described as a 'penetration effect' and limits the power capability of the system [2]. A way to design a better model would be using the generally accepted vernacular of Transmission Line, where the stepwise flux of ions within a pore can be described [52]. This is confirmed by the analysis of the Bode Plot obtained and by the non-linearity of the curves of the CCCD plot. Also, the inductance of the electrolyte, $L_{electrolyte}$, is extremely high (mH) for the dimension of the device and unlikely to be attributed only to the electrolyte behavior at AC frequencies. Coming up with a better model could be probably done with more time. Nevertheless, the values obtained with the present model are shown in Table 9.

Table 9 Estimated values of the parameters correspondig to each element of the EEC model applied to EIS.

PARAMETER	VALUE	ERROR	UNITS
$R_{CONTACT}$	63.55	8.62	Ω
L_{GAMRY}	507.70	504.10	nH
C_{DL}	57.90	553.30	µF
R_{CT}	6.77	14.77	Ω
$L_{ELECTROLYTE}$	149.70	388.00	mH
$C_{INTERFACE}$	1.26	0.63	mF
R_{SL}	338.90	193.20	Ω
C_{DIFF}	3.08	0.59	mF
GOODNESS OF FIT	181.90×10^{-6}	(-)	(-)

Through the values depicted in Table 9, the total capacitance, C_T, was calculated by making the sum of C_{diff}, C_{dl} and $C_{inteface}$ in series (C_T = 880.59 µF ± 304.42 µF). Due to the dominance of the order of magnitude of C_{dl}, the total capacitance is bound by it and the total capacitance is in the decimal case of the micrometers. Theoretically, it is like the $C_{interface}$ and C_{diff} do not actually exist. If the value of C_{dl} was accurate, we would be seeing a situation of overfitting, where block 3 and 4 should be removed, but in practice, that model does not fit the Nyquist Plot properly, since the nature of the errors seen are mainly attributed to the fact that the model is not appropriate. All values presented in Table 9 are modeled values except for $R_{contact}$ that can be obtained through the Bode Plot at maximum frequency. This value is approximately equivalent to ESR, so they are presented as being the same. In sum, the only relatively trusted value is the one of the ESR (80.96 Ωcm^{-2} ± 10.98 Ωcm^{-2}). In general, a small ESR is preferred for better electrochemical performance [33]. To obtain a low ESR the contact resistance between the active material coating and the current collector must be very low [2], [10]. However, one needs to keep

in mind that this ESR from an EIS test is often much smaller than that derived from the CCCD test and is therefore limited in describing the power performance of supercapacitor devices [6] [33].

As for the areal DL capacitance of the device, in comparison with literature, is much higher than for a parallel plate capacitor, that for a micrometer scale separation and a relative permittivity of 100 (water has a $\varepsilon \sim 80$), is of 0.1 $\mu F/cm^2$. The C_{dl} it is in the same scale of the DL capacitances of carbon electrodes (15 - 50 $\mu F/cm^2$) [45], with a value above average that is probably related with the presence of edge carbon atoms [6] originated by the exfoliation of graphite into graphene, this is, if we assume the value of C_{dl} (73.76 ± 704.84 μFcm^{-2}) to be correct. Fig. 11 represents the fractional residual error of the EEC used, that can give an insight about the source of possible errors from a statistical point of view.

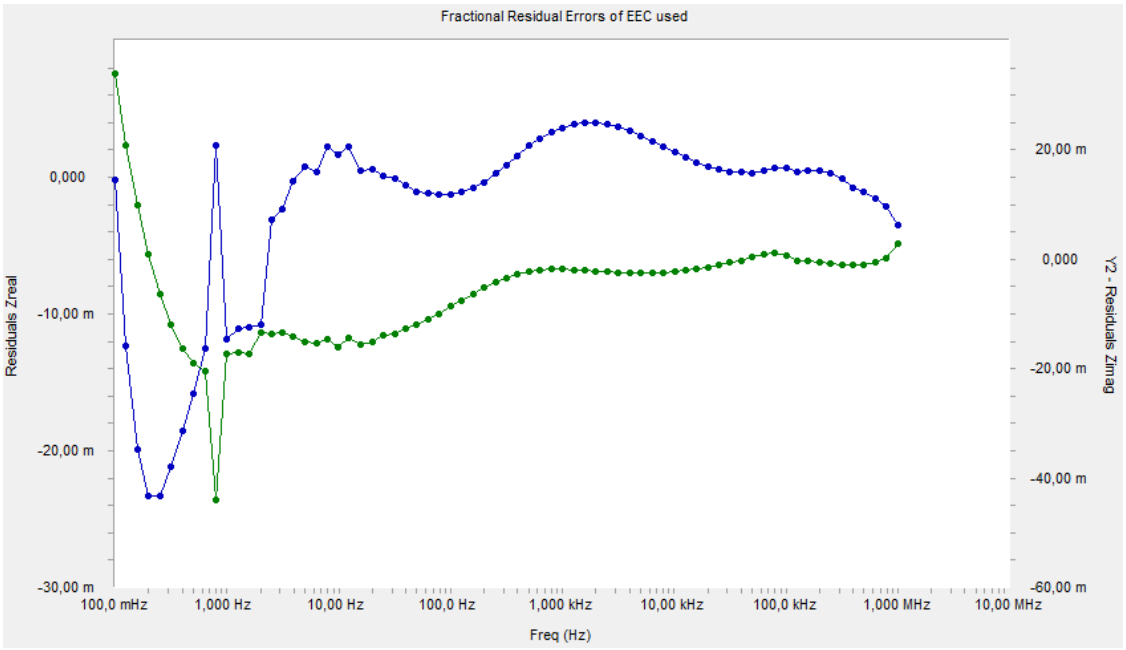

Figure 11 Fractional Residual Error of EEC used.

The Nyquist Plot

In Fig.12 its possible to observe the optimum fit to the Nyquist plot. The plot presents a depressed semi-circle in the high-middle frequency region (which represents the charge-transfer process) and a oblique straight line in the low frequency region (representing typical Warburg impedance e.g. ion diffusion) [53]. Here, the fit deviates weekly from the actual data points. For analytical applications, however, the equivalent circuit is often simplified by neglecting the Warburg impedance. This can be done by choosing a frequency range where no 45° line is observed in the Nyquist plot and the interfacial or bulk impedance is dominant [50], as it occurs in this case.

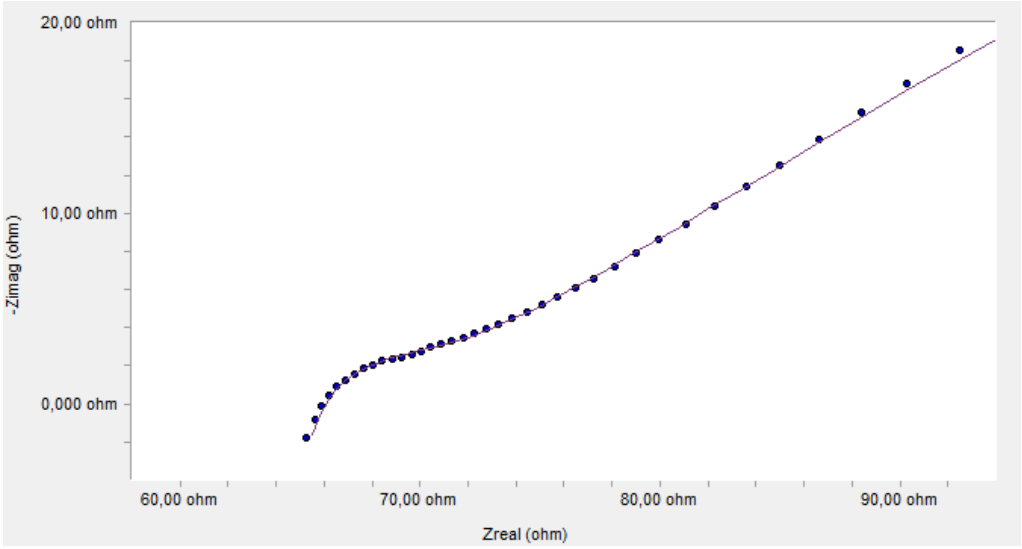

Figure 12 Nyquist Plot of the Ni@graphite device

The suppression of the semicircle in the Nyquist plot is due to the overlap of two different semicircles and indicates the contribution of two different resistive elements to the total impedance of the electrochemical cell. This is observed generally in the impedance plot due to the combination of a non-ideal capacitor element (CPE) and a resistor element in parallel. The semicircle in the high frequency region corresponds to the surface layer resistance (R_{sl}) or solid electrolyte interface (SEI) formation [53].

The Bode Plot

The bode plot of Ni@graphite obtained through the EIS test represent the real measurements taken by the potenciostat which is represented in Fig.13. A small voltage ripple amplitude (10 mV), with a variable frequency sweeping from 0.01 to 1 MHz, is applied to the device [54]. The current amplitude and phase with respect to the injected voltage allows to determine the module and the phase of the impedance (dark and light data points, respectively) as a function of the frequency.

The impedance elements on a Bode Plot can be identified by the phase angle: resistance is the only frequency independent element that presents a 0º phase shift, the others: capacitor (-90º), CPE (0 to-90º), inductance (0º- 90º) and Warburg (45º) are all frequency-dependent [50]. It is possible to observe that the device behaves like a CPE at low frequencies (100 mHz) and that gradually increases its resistive component as the frequency increases**,** reaching maximum resistance at 1 MHz. With respect to the module of the impedance (Z_{mod}), it decreases as the frequency increases, but as a fractional integral, revealing the non-linearity of the device. In a conventional capacitor, the decay is usually in the order of 20 dB/dec, a much steeper decay than what it can be observed here (e.g. between 1 and 10 Hz, Z_{mod} is not 10 times inferior). Regarding the EEC, above a certain frequency, the impedance of the capacitors become much smaller than the impedance of the resistors and since the capacitors are in parallel with the resistors, the capacitor acts as a short circuit and effectively removes the resistor from the circuit. At the highest frequencies, the impedance of the capacitor will also become much smaller than that of the resistor. Thus, the high frequency behavior of the device is controlled almost entirely by the resistive elements [55], as it can be observed in the Bode Plot.

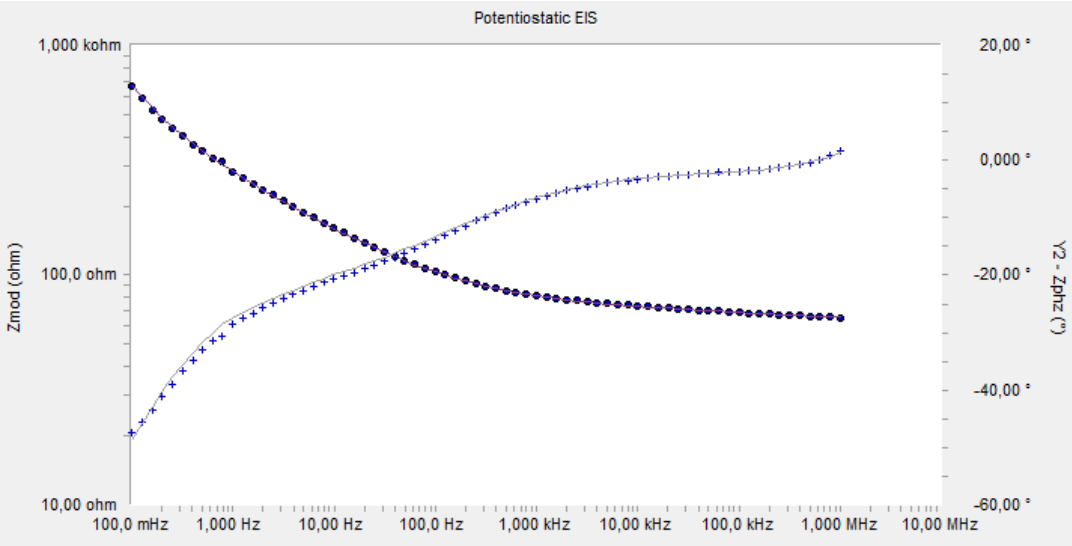

Figure 13 Bode Plot of Ni @graphite

4.10. Capacitance, Power and Energy Stored: comparing results

Capacitance is the property of an electric circuit or its element that permits it to store charge, defined as the ratio of stored charge to potential over that element or circuit (Q/V), but it can also be described by Equation 11,

$$C = \frac{\epsilon_r \epsilon_0 A}{d} \qquad \text{Equation 11}$$

where ϵr is the relative permittivity of the dielectric electrolyte (measured in V/m), ϵ_0, the vacuum permittivity ($\varepsilon_0 = 8.854 \cdot 10^{-12}$ F/m), d, the effective thickness of the double layer (DL) and A, the accessible surface area [57]. The energy density of a device is dependent on the capacitance and can be described by Eq.12 (in Wh or Wh Π^{-1}),

$$E_D = \frac{1}{2\Pi} C_T V_0^2 \qquad \text{Equation 12}$$

where C_T is the total capacitance, V is the maximum accessible potential window and Π the normalization factor [15], [33]. Alternatively, the normalization can also be carried out by the device mass m (kg), to provide a comparison for the compactness of energy and power devices [2], [6]. The power density can be calculated in one of two ways [3], [6].

$$P_D = \frac{\mathrm{E}}{\Delta \mathrm{t}} \qquad \text{Equation 13}$$

$$P_{max} = \frac{{V_0}^2}{4 R_{ES} \Pi} \qquad \text{Equation 14}$$

where Δt represents the discharge time (obtained via CV or galvanostatic charge/discharge) and the ESR is typically determined from galvanostatic charge-discharge [15], [33]. Equation 14 (P_{max}) provides a maximum available power and can only be realized when the load has the identical resistance as R_{ES}, often referred to as the matched load condition, but in practice, the load resistor often does not match, that is why Equation 13 gives the total power output during discharge. Both methods are acceptable; however, when discrepancies arise, Equation 13 should be used since it gives a more accurate picture of a real-world discharge situation.

Power is also inversely proportional to the total resistance of the cell, so a low resistance is desirable. The relationship between Power density (P_D) and Energy Density (E_D) for EDLCs is given by Equation 15 [3], [6].

$$\frac{E_D}{P_D} = 2R_{ES}C_T = 2\tau \qquad \text{Equation 15}$$

This equation indicates that the energy and maximum power densities are closely coupled by the cell time constant, τ. Although E_D can be increased by improving either the capacitance or operating voltage, raising the capacitance alone will simultaneously increase the time constant τ, leading to a less responsive cell, assuming ESR unchanged. Boosting the voltage can considerably enlarge both P_D and E_D, while still maintaining the same τ value.

Having the previous equations in mind, an overall evaluation of the measured (and calculated) parameters was made by comparing the results obtained in the electrical performance tests, presented in Table 10, with their respective normalized values. Normalization was made by the weight of active material, in kilograms, and by electrode area, in cm^{-2}.

The ESR value calculated from a CCCD test is generally more accurate than one obtained through the EIS test, however, since the non-linearity of the CCCD curves, it was not possible to calculate ESR through this method and consequently the maximum power. The time constant could only be determined by self-discharge, a test that was not performed. It was chosen instead to calculate power density using the deliverable energy obtained through discharge.

Table 10 Comparison of parameters results according to different tests. Normalization was made considering 26 µKg of active material, an area of 0.785 cm^2 and takig into account 1J = 2.7778×10^{-4} Wh

Parameters	CV	CCCD	Discharge
C_T [mF]	6.31 ± 0.07	56.63	25.84
ESR	(-)	63.55 ± 8.62 Ω (EIS)[12];	(-)
V_0 [V]	1.5	(-)	(-)
Capacity [µA-h]	(-)	(-)	6.78.
$E_{D\ cell}$ [µWh]	1.97 (7.10mJ)	17.70 (63.71mJ)	8.08 (29.07mJ)
$P_{D\ cell}$ [mW]	(-)	(-)	0.83
Normalized values			
C_S [Fg^{-1}]	0.24	2.17	0.99
C_T [$mFcm^{-2}$]	8.04	72.14	32.92
ESR [Ωcm^{-2}]	(-)	80.96 ± 10.98	(-)
E_D [$Wh \cdot kg^{-1}$]	0.076	0.68	0.31
E_D [$\mu Wh\ cm^{-2}$]	2.51 (9.05 mJ cm^{-2})	22.55 (81.16 mJ cm^{-2})	10.29 (37.03 mJ cm^{-2})

Regarding gravimetric capacitance, some authors subtract the amount of binder or other additives, others think it is more accurate to use the total mass of both dried electrodes [3]. In this case, normalization was made per gram of active material used. It was chosen not to report volumetric capacitance because precise estimation of electrode thickness is more difficult than precise estimation of electrode mass [2]**.** It also must be noted that experimental setup, mass loading, electrode thickness and electrode density (mass/volume) can alter the C_S value dramatically. In general, mass loading should be at least 5 mg/cm^2 and electrode thickness between 50–200 µm. Exceptions may be found for µ-supercapacitors in special applications [45]. Taking this into account, a two-electrode setup was used, and the calculated mass loading of the device was 17 mg/cm^2. With respect to net thickness of the active

[12] ESR from an EIS test is often much smaller than that derived from the Constant Current Charge Discharge (CCCD) test and is therefore limited in describing the power performance of supercapacitor devices [6] [33].

material on the current collector and electrode density values, they are not presented because the inherently difficulty of making those measurements.

5. CONCLUSIONS AND FUTURE PERSPECTIVES

5.1. Final conclusions

A new hybrid EES device was developed by using typical electrode materials for batteries (Nickel and carbon-derived electrodes) and a porous ceramic based separator (3YSZ), usually used as a dense, solid electrolyte. It was given utmost attention to the development of the graphite-derived electrode and to the fabrication of the porous separator. The electrographite was firstly mechanically exfoliated using a whetstone and only then subjected to chemical exfoliation using nine different agents. The one that resulted in a better graphite to graphene ratio resulted from the exfoliation in 25% water and 75% acetone in a sonication ice bath for 4h, with a particle concentration of 3 mg/ml. Graphite powder obtained through this method revealed to have a I_{2D}/I_G ratio of 0.90 in Raman spectra, indicating the presence of graphene. The carbon-derived electrode obtained by the mixture of exfoliated graphite and PVDF resulted in conductivities of $(1.17 \pm 0.18) \times 10^3$ S/m, a concentration of majority carriers of $-5.22 \cdot 10^{17} cm^{-2}$ and a mobility of 1.98 $cm^2 (V \cdot s)^{-1}$, for a percentage of active material of 27.93%.

Porous pellets of 3YSZ were fabricated through uniaxial pressing and the sintered according to eight different sintering chronograms. Open porosity was created by introducing different solid polymer particles (PVA, PVDF) with differing particle sizes and different ratios. Several 3YSZ:PVA ratios were studied, with applied forces of 1-11 kgF. The ratio 4:1 led to pellets with higher open porosities (36%) with chronogram 4 (C4). The 3YSZ pellet attained maximum open porosity (59%) with a ratio of 2:1.5 3YSZ nanopowder to PVDF using sintering chronogram 8.

The assembly of the device was made by casting both sides of the pellet with the viscous solution electrodes that were left to dry at room temperature, after which an electrolyte solution of 6M KOH was introduced laterally, being absorbed by the 3YSZ pellet. The performance of the device was measured by CV, CCCD and EIS, having attained capacitances between 6.31 and 56.63 m (0.24 - 2.17 Fg^{-1}). Energy densities were calculated considering an operating window of 1.5 V, as determined by the cyclic voltammograms. The reported values of capacitance and consequently of energy density are high for the dimensions of the device (9.05 mJ cm^{-2} - 81.16 mJ cm^{-2}). The curves in the CCCD plot reveal that the discharge is made almost instantly, revealing the high non-linearity of the device. It was also concluded that the model based in the Randles Cell is not adequate for the device assembled and that the Transmission Line Model should be used in future characterizations to allow the calculation of parameters accurately.

5.2. Future perspectives

To realize the full potential of the device, a better nickel electrode is needed to improve its charge storage capability and consequently its energy and power density. So, nickel in its pure form and the addition of an adequate binder in controlled proportions would be ideal. It should be considered making the nickel electrode porous for augmenting the SSA and therefore the capacitance. It would also be interesting to use electrolytes with lower ion radius (e.g. Lithium). Also with respect to the electrodes, an increased ratio of graphene to graphite content could be obtained by increasing the exfoliation time in the carbon-derived electrode, aggravating the graphene proprieties in the overall performance of the device. Wouldn't be a bad idea either, in a later stage, to dope the nickel electrode with pseudocapacitive material for increased energy density.

Improvements to the separator porosity would also be needed, since the separator used in this work didn't surpassed an open porosity of 49 %, while regular supercapacitors have separator porosities between 65 -75%. To reduce the thickness of the separator a different technique to fabricate the pellets would be preferred, particularly one that could combine applied temperature and pressure simultaneously. In this way, a wider range of porosities could be explored without addition of a solid polymer to the separator matrix. In addition, exploring the electric proprieties of 3YSZ as a porous separator as thoroughly as it is studied as for its dense form for solid electrolytes.

Finally, a fundamental understanding of the physical and chemical processes that take place in the interface between electrodes and electrolyte is needed to better model the physical phenomenon occurring in the device. Electrochemical analysis through EIS testing is not trivial, especially in new

devices that present high non-linearity. Modeling its physical behavior is still not an exact science and require mathematical approximations (Transmission Line Model). A better statistically analysis of the residual errors would also be of service.

In sum, with capacitances of this order there is no doubt that it is worth taking the investigation further, especially considering that these were attained by low-cost fabrication processes and with a nickel electrode that came from of a commercial source, that was not given any refinement in this first-stage exploratory work.

6. BIBLIOGRAPHY

[1] X. Luo, J. Wang, M. Dooner, and J. Clarke, “Overview of current development in electrical energy storage technologies and the application potential in power system operation q,” *Appl. Energy*, vol. 137, pp. 511–536, 2015.

[2] A. G. Pandolfo and A. F. Hollenkamp, “Carbon properties and their role in supercapacitors,” *J. Power Sources*, vol. 157, no. 1, pp. 11–27, 2006.

[3] F. Béguin, V. Presser, A. Balducci, and E. Frackowiak, “Carbons and electrolytes for advanced supercapacitors,” *Adv. Mater.*, vol. 26, no. 14, 2014.

[4] P. Simon, Y. Gogotsi, and B. Dunn, “Where Do Batteries End and Supercapacitors Begin?,” *Science (80-.).*, vol. 343, no. 6176, pp. 1210–1211, 2014.

[5] J. Goodenough, H. Abruña, and M. Buchanan, “Basic research needs for electrical energy storage,” *US Dep. Energy …*, p. 186, 2007.

[6] S. Zhang and N. Pan, “Supercapacitors performance evaluation,” *Adv. Energy Mater.*, vol. 5, no. 6, pp. 1–19, 2015.

[7] A. Burke, “R&D considerations for the performance and application of electrochemical capacitors,” *Electrochim. Acta*, vol. 53, no. 3 SPEC. ISS., pp. 1083–1091, 2007.

[8] L. Guan, L. Yu, and G. Z. Chen, “Electrochimica Acta Capacitive and non-capacitive faradaic charge storage,” *Electrochim. Acta*, vol. 206, pp. 464–478, 2016.

[9] J. Yan, Q. Wang, T. Wei, and Z. Fan, “Recent advances in design and fabrication of electrochemical supercapacitors with high energy densities,” *Adv. Energy Mater.*, vol. 4, no. 4, 2014.

[10] P. Simon and A. Burke, “Nanostructured carbons: Double-layer capacitance and more,” *Electrochem. Soc. Interface*, vol. 17, no. 1, pp. 38–43, 2008.

[11] W. Gu and G. Yushin, “Review of nanostructured carbon materials for electrochemical capacitor applications: Advantages and limitations of activated carbon, carbide-derived carbon, zeolite-templated carbon, carbon aerogels, carbon nanotubes, onion-like carbon, and graphene,” *Wiley Interdiscip. Rev. Energy Environ.*, vol. 3, no. 5, pp. 424–473, 2014.

[12] T. R. I. Cataldi and D. Centonze, “Development of a carbon composite electrode made from polyethylene and graphite powder modified with copper (I) oxide,” 1996.

[13] D. Bellido-milla, L. M. Cubillana-aguilera, M. El Kaoutit, M. P. Hernández-, and J. L. H. De Cisneros, “Recent advances in graphite powder-based electrodes,” pp. 3525–3539, 2013.

[14] M. Winter and R. J. Brodd, “What are batteries, fuel cells, and supercapacitors?,” *Chem. Rev.*, vol. 104, no. 10, pp. 4245–4269, 2004.

[15] P. Sharma and T. S. Bhatti, “A review on electrochemical double-layer capacitors,” *Energy Convers. Manag.*, vol. 51, no. 12, pp. 2901–2912, 2010.

[16] V. Augustyn *et al.*, “High-rate electrochemical energy storage through Li + intercalation pseudocapacitance,” vol. 12, no. June, pp. 1–5, 2013.

[17] J. Wang *et al.*, “Pseudocapacitive materials for electrochemical capacitors : from rational synthesis to capacitance optimization,” pp. 1–39, 2016.

[18] S. Luo, P. T. Hoang, and T. Liu, “Direct laser writing for creating porous graphitic structures and their use for flexible and highly sensitive sensor and sensor arrays,” *Carbon N. Y.*, vol. 96, pp. 522–531, 2016.

[19] Q. Ke and J. Wang, “Graphene-based Materials for Supercapacitor Electrodes - A Review,” *J. Mater.*, vol. 2, no. 1, pp. 37–54, 2016.

[20] S. Seal, “Graphene based materials : Past , present and future,” no. September 2016, 2011.

[21] W. Yang *et al.*, “Graphene in Supercapacitor Applications,” *Curr. Opin. Colloid Interface Sci.*, vol. 20, no. 5–6, pp. 416–428, 2015.

[22] J. Wang, X. Tong, and Y. Zhang, “Synthesis and characterization of graphene single sheets,” *Asian J. Chem.*, vol. 23, no. 5, pp. 2281–2283, 2011.

[23] Q. Ke and J. Wang, “Graphene-based materials for supercapacitor electrodes – A review,” *J. Mater.*, vol. 2, no. 1, pp. 37–54, 2016.

[24] J. Kim, J. Lee, C. Yoo, K. Lee, and W. Lee, “Low-cost and energy-efficient asymmetric nickel electrode for alkaline water electrolysis,” *Int. J. Hydrogen Energy*, vol. 40, no. 34, pp. 10720–10725, 2015.

[25] E. G. VandeBoshe, “The Potential of the Nickel Electrode,” University of Maryland, 1927.

[26] E. M. Rus, D. M. Constantin, and L. Oniciu, “Structural and Electrochemical Characteristics of Sintered Nickel Electrodes,” vol. 72, no. 1, pp. 25–41, 1999.

[27] H. Shimojo, Fuyuki ; Okabe, Tseuneyasu ; Tachibana, Fumio ; Kobayashi, Michisuke ;Okazaki, “Molecular Dynamics Studies of Yttria Stabilized Zirconia. I.Structure and Oxygen Diffusion,” vol. 61, no. 8, pp. 2848–2856, 1992.

[28] M. F. Kibria, “STUDIES OF THE NICKEL ELECTRODE,” vol. 21, no. 3, 1996.

[29] C. Liu, Z. G. Neale, and G. Cao, “Understanding electrochemical potentials of cathode materials in rechargeable batteries,” *Biochem. Pharmacol.*, vol. 0, no. 0, 2015.

[30] A. J. Bard, L. R. Faulkner, E. Swain, and C. Robey, *Electrochemical Methods, Fundamentals and Applications*. John Wiley and Sons, Inc, 2001.

[31] H. Li, G. Weng, C. Ying, V. Li, and K. Chan, “Electrochimica Acta Three electrolyte high voltage acid – alkaline hybrid rechargeable battery,” *Electrochim. Acta*, vol. 56, no. 25, pp. 9420–9425, 2011.

[32] D. I. B. Erndt, B. Ag, and F. Republic, “Ullmann’s Encyclopedia of Industrial Chemistry.” 2012.

[33] S. Zhang and N. Pan, “Supercapacitors performance evaluation,” *Advanced Energy Materials*, vol. 5, no. 6. 2015.

[34] B. Marinho, M. Ghislandi, E. Tkalya, C. E. Koning, and G. De With, “Electrical conductivity of compacts of graphene , multi-wall carbon nanotubes , carbon black , and graphite powder,” *Powder Technol.*, vol. 221, pp. 351–358, 2012.

[35] C. M. F. Calixto, R. K. Mendes, A. C. De Oliveira, L. A. Ramos, P. Cervini, and É. T. G. Cavalheiro, “Development of graphite-polymer composites as electrode materials,” *Mater. Res.*, vol. 10, no. 2, pp. 109–114, 2007.

[36] B. Kumar, C. Chen, C. Varanasi, and J. P. Fellner, “Electrical properties of heterogeneously doped yttria stabilized zirconia,” vol. 140, pp. 12–20, 2005.

[37] A. Eichler, “Tetragonal Y-doped zirconia : Structure and ion conductivity,” vol. 64, pp. 1–8, 2001.

[38] O. Cosme, R. Moreira, D. A. Silva, C. Jorge, and E. Rodríguez, “Microestrututra e propriedades elétricas da zirconia dopada com óxidos mistos de terras raras para aplicação como eletrólito sólido em sensores de oxigénio,” Universidade de Brasília, 2013.

[39] P. D. C.Pascual, J.R Hurado, “Electrical behaviour of doped-yttria stabilized zirconia ceramic materials,” *Mater. O F*, vol. 8, no. 1980, pp. 1315–1322, 1983.

[40] M. Yi, Z. Shen, X. Zhang, and S. Ma, “Achieving concentrated graphene dispersions in water / acetone mixtures by the strategy of tailoring Hansen solubility parameters w .,” vol. 46, 2013.

[41] M. Wall, “The Raman Spectroscopy of Graphene and the Determination of Layer Thickness,” *Thermo Sci.*, p. 5, 2011.

[42] I. Childres, L. A. Jauregui, W. Park, H. Cao, and Y. P. Chen, “R AMAN S PECTROSCOPY OF G RAPHENE AND.”

[43] B. Neha, K. S. Manjula, B. Srinivasulu, and S. C. Subhas, “Synthesis and Characterization of

Exfoliated Graphite / ABS Composites," vol. 2012, no. October, pp. 74–78, 2012.

[44] M. S. Dresselhaus, *Intercalation in Layered Materials*, Nato ASI S. Cambridge, Massachusetts: Springer, 1986.

[45] B. Hsia, "Materials Synthesis and Characterization for Micro-supercapacitor Application," Berkeley, University of California, 2013.

[46] H. Wang and L. Pilon, "Electrochimica Acta Physical interpretation of cyclic voltammetry for measuring electric double layer capacitances," *Electrochim. Acta*, vol. 64, pp. 130–139, 2012.

[47] M. D. Stoller and R. S. Ruoff, "Best practice methods for determining an electrode material's performance for ultracapacitors," pp. 1294–1301, 2010.

[48] M. Rajkumar, C. Hsu, T. Wu, M. Chen, and C. Hu, "Advanced materials for aqueous supercapacitors in the asymmetric design," *Prog. Nat. Sci. Mater. Int.*, vol. 25, no. 6, pp. 527–544, 2015.

[49] M. A. Macdonald and H. A. Andreas, "Electrochimica Acta Method for equivalent circuit determination for electrochemical impedance spectroscopy data of protein adsorption on solid surfaces," *Electrochim. Acta*, vol. 129, pp. 290–299, 2014.

[50] F. Lisdat and D. Schäfer, "The use of electrochemical impedance spectroscopy for biosensing," pp. 1555–1567, 2008.

[51] A. Bardos, R. N. Zare, and K. Markides, "Inductive behavior of electrolytes in AC conductance measurements," vol. 402, pp. 274–278, 2005.

[52] G. Instruments, "Use of Transmission Lines for Electrochemical Impedance Spectroscopy Theory and Application of Transmission Line Models to High Surface Area Electrodes," 2017. .

[53] E. O. Ortiz-quiles *et al.*, "Enhanced Structural Integrity and Electrochemical Performance of AlPO 4 - Coated MoO2 Anode Material for Lithium-Ion Batteries," no. March 2014, 2015.

[54] F. Rafik, H. Gualous, R. Gallay, A. Crausazl, and A. Berthon, "Supercapacitors characterization for hybrid vehicle applications," 2006.

[55] Princeton Applied Research, "Application Note AC-1. Subject : Basics of Electrochemical Impedance Spectroscopy Overview." .

[56] M. Rajkumar, C. Hsu, T. Wu, M. Chen, and C. Hu, "Advanced materials for aqueous supercapacitors in the asymmetric design," *Prog. Nat. Sci. Mater. Int.*, pp. 1–18, 2015.

[57] K. Omar, M. D. Johan Ooi, and M. M. Hassin, "Investigation on Dielectric Constant of Zinc Oxide," *Mod. Appl. Sci.*, vol. 3, no. 2, pp. 110–116, 2009.